An observational approach to stars embedded in the circumstellar matter with a new high resolution spectro-polarimeter

2014

Takayuki Arasaki

Abstract

Young stellar objects (YSO) such as T Tau star and Herbig Ae/Be star, and evolved stars after the main-sequence such as Wolf-Rayet often have the circumstellar matters, which are formed by the mass loss process, the mass accretion from the companion, and so on. Since these circumstellar matters are thought to be not spherically distributed with a complicated velocity field, they should strongly influence on stellar evolution. Therefore, it is extremely important to obtain information on the spatial distribution and the velocity field for the study on stellar evolution. High resolution spectro-polarimetry is a unique observational technique, because it can determine these three-dimensional spatial distribution and velocity field simultaneously for a stellar object which cannot be spatially resolved due to the limitation by the seeing or diffraction. Actually, high resolution spectro-polarimetry has provided various impressive results for a couple of decades. These high resolution spectro-polarimetries began in 1990s when astronomers acquired the means for collecting a much number of photons from faint objects due to the building 8–10 -m class telescopes and the polarization of the highly sensitive detector such as CCD. For 8-10 -m class telescopes, a few spectro-polarimeters such as the Focal Reducer and low dispersion Spectrograph (FORS2) on the Very Large Telescope (VLT) and the Faint Object Camera and Spectrograph (FOCAS) on the Subaru telescope are commissioned. Since they are multi-purpose type instruments with a polarization module, they cannot maintain a high accurate polarimetry. In addition, there was an issue that there is the “ripple” in highly resolved spectra using the Pancharatnam-type (super-achromatic) wave plate, which has been widely used for astronomical polarimeters, resulting in a terrible degradation of polarimetric accuracy. Finally, this ripple problem

was overcome by a new non-ripple super-achromatic wave plate (Ikeda *et. al*. 2003) and Fresnel rhomb (Donati *et al*. 2006). A few fiber-fed type spectro-polarimeters with a large echelle high resolution spectrograph, such as Echelle SpectroPolarimetric Device for the Observation of Stars (ESPaDOnS), were built because of usability of the large format CCD and the high efficient optical fiber. However, the fiber-fed type spectro-polarimeter has a disadvantage on the stability for absolute polarimetry because the throughput and the coupling efficiency vary in night by night due to the bending and the slight mechanical displacement of the fiber. Therefore, we develop a new high resolution spectro-polarimeter for 1–2 -m telescopes, VESPolA, which can achieve a high polarimetric accuracy and a high stability in polarimetry, simultaneously.

The line widths of emission stars such as T Tau stars and WR stars often fall within δv = 100–300 km s^{-1}. Therefore, the spectral resolution is determined to be δv = 10–30 km s^{-1} to resolve those line profiles sufficiently. The wavelength coverage for a single exposure is required to be at least $\delta\lambda > 150$ nm to obtain the several material lines simultaneously. The polarimetric accuracy must be $\delta P \sim 0.1\%$ because the polarization of astronomical objects are often 1% or less. We proposed a solution using an echelle spectrograph and a non-ripple super-achromatic half-wave plate to meet these requirements. In addition, we decided to use only originally designed achromatic-lens systems before a polarization analyzer to reduce the instrumental polarization. As a result, we obtained an optical design to achieve a high polarimetric accuracy of $\delta P < 0.1\%$ for linear polarization with a spectral resolution of R = 8,000 and cover a wide wavelength of $\delta\lambda$ = 150–250 nm in a single exposure.

For polarization analysis, VESPolA adopts the “four-angles method. This method enables highly accurate polarimetry because it can cancel the difference of the weather condition among images taken in different timings, and the difference of the efficiency difference between the o- and e-rays in the optical system without additional calibration spectra. For high resolution spectro-polarimetry of line profile, the precision of the wavelength calibration is very important. Owing to the carefully wavelength calibration, we achieved an accuracy of ± 0.06 Å which does not produce any fake polarization features in polarization line spectra.

We verified the optical performances of the assembled VESPolA, mounted on the 1.3 -m Araki-telescope at the Koyama Astronomical Observatory of Kyoto Sangyo University, from November 2012 to November 2013. With several polarimetric standard stars, UPs and SPs, and a spectroscopic standard (SS) star for evaluating the polarimetric accuracy and the optical throughout, we confirmed that VESPolA achieved a spectral resolution $7{,}750 < R < 8{,}250$, with a polarimetric accuracy of $\delta P \sim 0.1\%$ for linear polarization and a limiting magnitude of $m_v = 7.8$ mag with $\delta P < 0.1\%$ and an integration time of 4 hours.

V339 Del (= Nova Del 2013) is a FeII class fast nova which was discovered on 2013 Aug. 14. We carried out a monitoring observation of V339 Del using VESPolA in the early phase including before the maximum (t = -1d). We confirmed from P Cygni profiles in FeII, SiII, HeI, OI, and Balmer lines that the nova wind already has just before the maximum. In addition, the SiIIλλ6347, 6371, Hα, and OIλλ7477, 7774 lines show the intrinsic polarizations which are different from that of the continuum. In particular, only SiIIλλ6347, 6371 show prominent polarization in the pre-maximum phase. This polarization would reflect a patched or biasedly distribution of the SiII region on

the pseudo-photosphere. This suggests that the first nuclear reaction is locally ignited in the bottom of hydrogen layer of the WD atmosphere, into which the Si species is diffused. This Si species is not generated by the TNR but is originally included in accreting gas from the companion.

As above mentioned, we succeeded in development of high resolution spectro-polarimeter, VESPolA, for study on spatial distribution and velocity field of circumstellar matters. It is confirmed by the study with line polarization of a nova in the early phase that it provide competent performances for studies on the circumstellar environment of the YSOs, evolved stars, and transit objects.

CONTENTS

1. Introduction

1.1. Approach to circumstellar environment with high resolution spectro-polarimetry

Stars often have the circumstellar matters in any evolutional stages seen in young stellar objects (YSO) and evolved stars after main sequence, which are formed by the mass loss process, the mass accretion process from the companion, and so on. The circumstellar matter is thought to have a complicated spatial distribution with a characteristic velocity field. T Tau star and Herbig Ae/Be star in pre-main sequence are known that they have a large scaled accretion disk resulted from the collapse of a molecular cloud core (e.g., Calvet *et al*. 1994, Takami *et al*. 2001). Luminous Blue Variables (LBVs) and Wolf-Rayet stars (WR stars) that are massive stars coming close to the final stage show the time variation of the brightness in time scale from a few hours to a few hundred years by a continuous massive stellar wind or a temporal mass loss event called as eruptions (e.g., Smith 2008). Dwarf nova, Nova, and Ia type SN are known as a sudden outburst phenomenon that is related to the accretion transfer process from the companion star (e.g., Nomoto *et al*. 1994), although a double degenerate stars scenario is also a widely-accepted theory as the progenitor of Ia type supernovae (e.g., Hillebrandt & Niemeyer 2000). Since the circumstellar matters are thought to be not spherically distributed that is having a complicated velocity field, they should greatly influence on the process of stellar evolution. Therefore, it is very important to obtain information on the spatial distribution and the velocity field of these stars for the study on stellar evolution. However, in most cases, the circumstellar nebula around stars cannot be spatially resolved by direct imaging observations. For example, if a star at the distance of 1 kpc have a circumstellar with disk of a diameter of

~100 AU, the appearance size is only 0.1 arcsec. It have to a resolution of about 10 AU (0.01") to discuss the internal structure of the disk. Even the Hubble Space Telescope (HST), whose resolving power is 0.04" at V-band, can resolve it. Traditionally, the spatially distribution has been obtained with only radial velocities a by high resolution spectra and a model reproducing the physical condition of the circumstellar environment (e.g., Smith & Hartigan 2006). However, this method cannot give a unique solution with only radial velocity and strongly depends on the used model. The high resolution spectro-polarimetry has a capability of overcoming these disadvantages.

High resolution spectro-polarimetry is a unique observational technique because it can determine three-dimensional geometry and the velocity field on the circumstellar environment. Gas and dust particles, which are non-spherically distributed in the circumstellar region, scatter light from the central star, resulting in polarization. Moving scatters result in a wavelength shift of the incident light, and characteristic polarization profiles $P(\lambda)$ and $\theta(\lambda)$ are produced across the absorption and emission lines. We can extract the density distribution and the three-dimensional velocity filed of the circumstellar region from the polarization spectra of various lines, even if the circumstellar region is spatially unresolved due to the limitation by seeing or diffraction (e.g., Wood *et al*. 1993 and Pontefract *et al*. 2000). As mentioned in the following, high resolution spectro-polarimetry has provided various interesting results for a couple of decades with the state-of-art spectro-polarimeters gradually developed after 1990s. Pereyra *et al*. (2009) carried out spectro-polarimetry of B[e] star, GG Car. They con-

cluded from an intrinsic polarization along Hα line that GG Car has a counter-clockwise rotating disk. The rotational direction cannot be estimated with other method. Taylor *et al*. (1991) reported a result of spectro-polarimetry of P Cyg with HPOL spectro-polarimeter mounted on 0.9 -m telescope at Pine Bluff Observatory. From the time variation of polarization of Balmer lines and HeIλ5876Å, they found that P Cyg has a non-spherical geometry which could be formed by plumes or blobs. Schmid & Schild (1990) reported a result of spectro-polarimetry of unidentified line λλ6825, 7087Å of symbiotic star He2-38. They detected intrinsic linear polarizations in these lines. This strongly supports that these lines come from Raman scattering by neutral hydrogen of O_{VI} λλ1032, 1038 lines emitting in the neighboring region of the WD, which is originally proposed by Schmid (1989). This observation made an end on a debate over several decades among a number of astronomers. After then, Schmid & Schild (1994) confirmed this hypothesis by the detection of linear polarizations in Southern 15 symbiotic stars. Since Raman scattered lines show strong polarization, they were used to demand the orbital elements of symbiotic stars by monitoring the variation of polarization of Raman-scattered lines (Schmid & Schild 1997, Harrie & Howarth 1996, 2000). Ikeda *et al*. (2004) discovered the other Raman scattered lines in Hα wing with a high resolution spectro-polarimetry, which would be scattered by a neutral hydrogen of Ly*β* lines. Vink *et al*. (2003) and Akitaya *et al*. (2009) reported spectro-polarimetries of T Tau star, RY Tau with ISIS (Rasilla *et al*. 1993) mounted on the 4.2 -m William Herschel Telescope (WHT) and LIPS (Ikeda *et al*. 2003) mounted on the Cassegrain focus of the University of Hawaii 2.2 -m telescope, respectively. They concluded from an intrinsic polarization along Hα line and forbidden lines (e.g., [OI]λλ5577, 6300, 6364 and [NII]λ6583)

that RY Tau star has a rotating disk which scatter their permitted and forbidden lines. Harrington & Kuhn (2009) reported spectra by high resolution spectro-polarimetry for six post-AGB stars and three RV Tau stars with ESPaDOnS (Donati 2003) mounted on 3.6 -m Canada-France-Hawaii Telescope (CFHT) and HiVIS (Harrington *et al*. 2006) on 3.7 -m AEOS telescope. These high resolution spectro-polarimetry (R = 68,000 and R = 13,000, respectively), have never been carried out before using night telescopes. They detected intrinsic polarization across the Hα line in eight of nine stars. 89 Her of post-AGB star and AC Her of RV Tau star show time variations of the polarization profiles.

As just described, there are several interesting results by high resolution spectro-polarimetry. However, there had been very few observations for a aiming at the time variation of polarization profile, because spectro-polarimeters often are often attached to large telescopes for which much observation time is not easy to allocate and/or the poor polarimetric accuracy of these instruments prevents various science with high resolution spectro-polarimeter. In addition, most observations are limited to a single line such as Hα because of the narrow wavelength coverage of the instruments. If we obtain polarization profiles of several lines simultaneously, we could obtain a comprehensive understanding on the ionized gas by comparing with those polarization profiles each other. A spectro-polarimeter and an exclusive use telescope are needed for driving forward these fruitful studies with high resolution spectro-polarimetry.

1.2. A brief history of high-resolution spectro-polarimeters

In this section, we focus on the instruments to realize the spectro-polarimetry that were introduced in the previous section. These high resolution spectro-polarimetries began in 1990s and when astronomers acquired the means for collecting a much number of photons from faint objects due to the building 8–10 -m class telescopes and the popularization of the highly sensitive detector such as CCD. It is theoretically necessary a much number of photons because high resolution spectro-polarimetry needs to observation of S/N = 1,000 ($\delta P < 0.1\%$).

The Intermediate spectrograph and Imaging System (ISIS) instrument (Rasilla *et al*. 1993) is a representative instrument in the dawn of high resolution spectro-polarimetry. ISIS attached to the 4.2 -m William Herschel Telescope (WHT) provided some of the best early spectro-polarimetry data (e.g., de Diego *et al*. 1994, Dhillon & Rutten 1995). The original ISIS consisted of an imager, a spectrometer, and a spectro-polarimetric mode was realized by installing a polarization module in the optical train. ISIS employed a savart plate as the analyzer, which produces two polarized orthogonal images (ordinary and extra-ordinary images) on the focal plane. ISIS can observe linearly and circularly polarized spectra with $4{,}000 < R < 9{,}000$ over a wavelength range of 300–1,100 nm. However, the spectral coverage in a single exposure was limited to $\delta\lambda \sim 40$ nm because it used first-order reflective gratings.

The importance of high resolution spectro-polarimetry has increased since the late 1990s because it became possible to collect a larger photon flux owing to the appearance of building 8–10 -m telescopes.

The Focal Reducer and low dispersion Spectrograph (FORS2) on the Very Large Telescope (VLT) (Seifert

et al. 2000) and the Faint Object Camera and Spectrograph (FOCAS) on the Subaru telescope (Kashikawa *et al*. 2002) are multi-purpose instruments that include a spectro-polarimetric mode in the visible wavelength region. A polarization modulator and a Wollaston prism as analyzer are installed near the pupil, where the collimated beam diameter was a minimum. FORS2 can obtain linear and circular polarization spectra $260 < R < 2{,}600$ in the wavelength range of 130–500 nm using several types of grisms, and FOCAS can obtain high-dispersion linear and circular spectra with $5{,}500 < R < 7{,}500$ via a volume phase holographic (VPH) grism (Ebizuka *et al*. 2011). Both instruments have multi-object spectro-polarimetric modes, realized with multi-slit masks located on the focal plane of the telescope. However, because these multi-purpose spectro-polarimeters must have polarization modulators in the central position of the optical train, the instrumental polarization generated by the upstream lenses and or the other optical elements forward of the modulator often degrades the final polarization accuracy.

With these multi-purpose spectro-polarimeters mounted on the Cassegrain focus, it is difficult to achieve both high dispersion and wide wavelength coverage simultaneously because it often requires first-order grisms for compatibility with the imaging mode. These problems were solved by the development of the fi-ber-fed echelle spectro-polarimeter, with which stellar images at the Cassegrain focus can be fed to an echelle type high resolution spectrograph located on the Coude room or Nasmyth platform via optical fibers. How-ever, this type of spectro-polarimeter has a disadvantage in that the obtained polarization is unstable due to

the coupling losses or curvature losses of the fiber. One of the first fiber-fed high resolution spectro-polarimeters is the Multi-Site Continuous Spectroscopy (MuSiCoS) (Donati *et al*. 1999) attached to the Telescope Bernard Lyot (TBL). MuSiCoS employs a savart plate at the Cassegrain focal plane, which produces two orthogonal polarized images. These images are fed to an echelle spectrograph located on the floor of the telescope dome via two multi-mode optical fibers. It achieves both linear and circular spectro-polarization with $R \sim$ 35,000 in the range of 390–870 nm; however, a new technical problem is faced in achieving a high-resolution spectro-polarimeter, namely ripple, which is a high-frequency modulation in the spectra that degrades the polarization accuracy because of the time variation of the ambient temperature (Donati *et al*. 1999). MuSiCoS is superseded by NARVAL high resolution spectro-polarimeter after 2008 (Silvester *et al*. 2012).

The Pancharatnam-type wave plate has been widely used as a modulator in polarimeters since the 1960's. It consists of three SiO_2 thin plates and three MgF_2 thin plates, which are alternately stacked. Because SiO_2 and MgF_2 have the different refractive indices, multiple Fresnel reflections are generated at the boundaries of two plates, resulting in an interferometric modulation pattern, i.e., ripple, in the high dispersion spectra. Donati's group developed a high-resolution linear/circular spectro-polarimeter, Echelle SpectroPolarimetric Device for the Observation of Stars (ESPaDOnS), using a Fresnel rhomb as a modulator that can, in principle, completely eliminate ripple (Donati *et al*. 2006). ESPaDOnS operates at the Canada-France-Hawaii Telescope (CFHT). A spectral resolution of R = 65,000 was achieved, which is the highest to data for spectro-polarime-

ters in night telescopes. Although the Fresnel rhomb overcomes the ripple, it has not been widely used because (i) it is difficult to image a large field of view due to the long optical path of Fresnel rhomb, (ii) technologies are not yet available to produce a large Fresnel rhomb, and (iii) it generates a large deflection of the exiting light due to the rotation, resulting in the degradation of the spectra on the detector.

Alternatively, Snik *et al*. (2011) realized a new high resolution spectro-polarimeter with non-ripple by installing a polarization module into a visible high resolution spectrometer with $R \sim 110{,}000$, High-Accuracy Radial velocity Planetary Searcher (HARPS), at the 3.6 –m ESO telescope. This polarization module employs newly-invented super-achromatic wave plate as the modulators. Since these wave plates consists of multiple PMMA layers (with a refractive index of $n = 1.49$), multiple reflections at the boundaries between the layers, are inhibited, and so in principle, ripple should be eliminated in the spectrum. This wave plate was first employed on the Line Polarimeter and Spectrograph (LIPS) visible high resolution spectro-polarimeter (Ikeda *et al*. 2003), which is a prototype of VESPolA. A similar spectro-polarimeter using PMMA retarders, PoTsdam Echelle Polarimetric and Spectroscopic Instrument (= PEPSI), has been developed for on the Large Binocular Telescope (LBT) (Ilyin *et al*. 2011). PEPSI is a fiber-fed high resolution echelle spectro-polarimeter with a highly accurate ($\delta P \sim 0.1\%$) and high-resolution ($R = 120{,}000$) spectro-polarimeter.

Table 1.1 lists the above various spectro-polarimeters.

	Telescope	Spectral range (nm)	Spectral Resolution	Disperser	Modulation type
ISIS	4.2-m William Herschel Telescope	300–1000	4,000–9,000	1st-order reflective grating	Super achromatic 1/4-wave and 1/2-wave plate coupled with a savart plate
FORS2	8.2-m Very Large Telescope	330–1100	260–2,600	1st- order grism	Super achromatic 1/4-wave and 1/2-wave plate coupled with a Wollaston prism
FOCAS	8.2-m SUBARU Telescope	350–1200	250–3,000	1st- order grism &VPH	Super achromatic 1/4-wave and 1/2-wave plate coupled with a Wollaston prism
MuSiCoS	2-m Telescope Bernard Lyot	390–870	35,000	Fiber-fed + echelle	Super achromatic 1/4-wave and 1/2-wave plate coupled with a savart plate
ESPaDOnS	3.6-m Canada–France–Hawaii Telescope	370–1050	65,000	Fiber-fed + echelle	1/4-wave and 1/2-wave Fresnel retarders coupled with a Wollaston prism
HARPSpol	3.6-m ESO Telescope	380–690	110,000	Fiber-fed + echelle	PMMA zero-order 1/4-wave and 1/2-wave plate coupled with a Foster prism
PEPSI	2 × 8.4-m Large Binocular Telescope	383–907	120,000	Fiber-fed + echelle	PMMA zero-order 1/4-wave plate coupled with a Foster prism
VESPolA (this thesis)	1.3-m Araki Telescope	400–850	8,000	Echelle	PMMA zero-order 1/2-wave plate coupled with a double Wollaston prism

Table 1.1 The specifications of number of existing spectro-polarimeters

1.3. Purpose of this paper

As above mentioned, high resolution spectro-polarimetry is effective method to study the spatial distribution and velocity fields of the circumstellar environment. Furthermore, it is thought that much information is provided by aiming at the time variation of polarization profile. However, most of the spectro-polarimeters which can achieve a high polarimetric accuracy and a broad wavelength range simultaneously are not exist. We developed high resolution spectro-polarimetry (= VESPolA) for 1–2m class telescope that such as observation was enabled by adopting a technique of high accuracy and high resolution to win developed for large telescope. Even we carried out a monitoring observation of nova using VESPolA in the early phase, and obtained knowledge about the non-spherical geometry by wind.

In section 2, we describe the design of a new high resolution spectro-polarimeter, VESPolA, and in section 3, we describe the reduction method of observed data. In section 4, we evaluate the overall performance of the polarization accuracy and the limited magnitude of VESPolA, and in section 5, we show a scientific result of nova using VESPolA.

2. Development of a new high resolution spectro-polarimeter

2.1. Design concept of VESPolA

The major scientific aim of his project is to investigate the time variation of stars, including transient phenomena and variable stars. We aim to obtain information on the density distributions and velocity fields of the circumstellar environment of these stars. Given that the degree of polarization of the light from the stars is typically 1% or less, the polarimetric accuracy must be less than $\delta P = 0.1\%$ for linear polarization to detect polarization variations via changes in the circumstellar environment. Furthermore, the stability of the instrument is important to evaluate the polarization variations on a night-by-night basis. The emission lines of stars, including WR stars, Be stars, Herbig Ae/Be stars, and T Tau stars, which evolve rapidly on HR diagram, often have a line width of ~300 kms^{-1} (e.g., Stahl *et al*.1993, and Catanzaro 2013). Therefore, the instrument should have a velocity resolution of $\delta v < 50$ km s^{-1} to resolve the line profile of the emission lines. The spectrum obtained in a single exposure should cover at least $150 < \delta\lambda < 200$ nm to study the three-dimensional structure of the ionized nebula by analyzing multiple emission lines simultaneously. To achieve these requirements, we adopted a cross-dispersed-type spectrograph with an echelle grating for the spectrometer unit of VESPolA. In many cases, echelle-type spectropolarimeters are located on stable floors and the stellar light is fed via a fiber-optics system on the telescope focal plane (as is the case with MuSiCoS and ESPaDOnS). However, VESPolA is directly attached to the Cassegrain focus, and fiber-fed units (which degrade the polarimetric accuracy due to the instability of the throughput and the coupling efficiency) are not used. The reductions in size and weight of the instrument are additionally needed

for avoiding bending of the instrumental body. We aim to achieve high polarimetric accuracy via the followings; (i) the modulator was installed just before the entrance slit; (ii) a non-ripple super-achromatic half-wave plate was used as the modulator to prevent ripple which occur on a wave-plate boundary surface of each layers; and (iii) an non-reflective dielectric entrance slit was employed, not reflective mirror, at the entrance slit to minimize the instrumental polarization. Table 2 lists a summary of the specifications of the Araki-telescope and of VESPolA.

	Items	Specifications
Instrument	Spectral resolution	$R \geq 6{,}000$ ($\delta v < 50$km s^{-1})
	Spectral coverage	$400 < \delta\lambda < 850$ nm (for a single exposure: $\delta\lambda \geq 150$–250 nm)
	Polarimetric accuracy	$\delta P < 0.1\%$
	Position angle accuracy	$\delta\theta < 1°$
Telescope	Telescope diameter	$D = 1.3$ -m
	Telescope *f*-number	*f*/10 at Cassegrain focus

Table 2.1 Basic specifications of the Araki-Telescope and VESPolA

2.2. Optics

The optical layout of VESPolA is shown in Figure 2.1. An instrument consists of three units: a calibration unit, a polarization analysis unit, and a spectrometer unit. The calibration unit is equipped with a HCT-lamp for wavelength calibration, a Glan-Talor prism to correct for instrumental depolarization (see section 5.2.2), a rotatable half-wave plate as the modulator, and an auto-guidance system. The collected light from the telescope passes through the entrance slit, which is located at the top of the polarization analysis unit, and is split into two linearly polarized orthogonal rays (ordinary and extra-ordinary rays) using a double Wollaston prism. In the spectrometer unit, a cross disperser and an echelle grating disperse the two polarized rays and form a two-dimensional echellogram spectrum on the CCD detector via a camera lens. Table 2.2 lists a summary of the parameters of the optical elements employed in VESPolA.

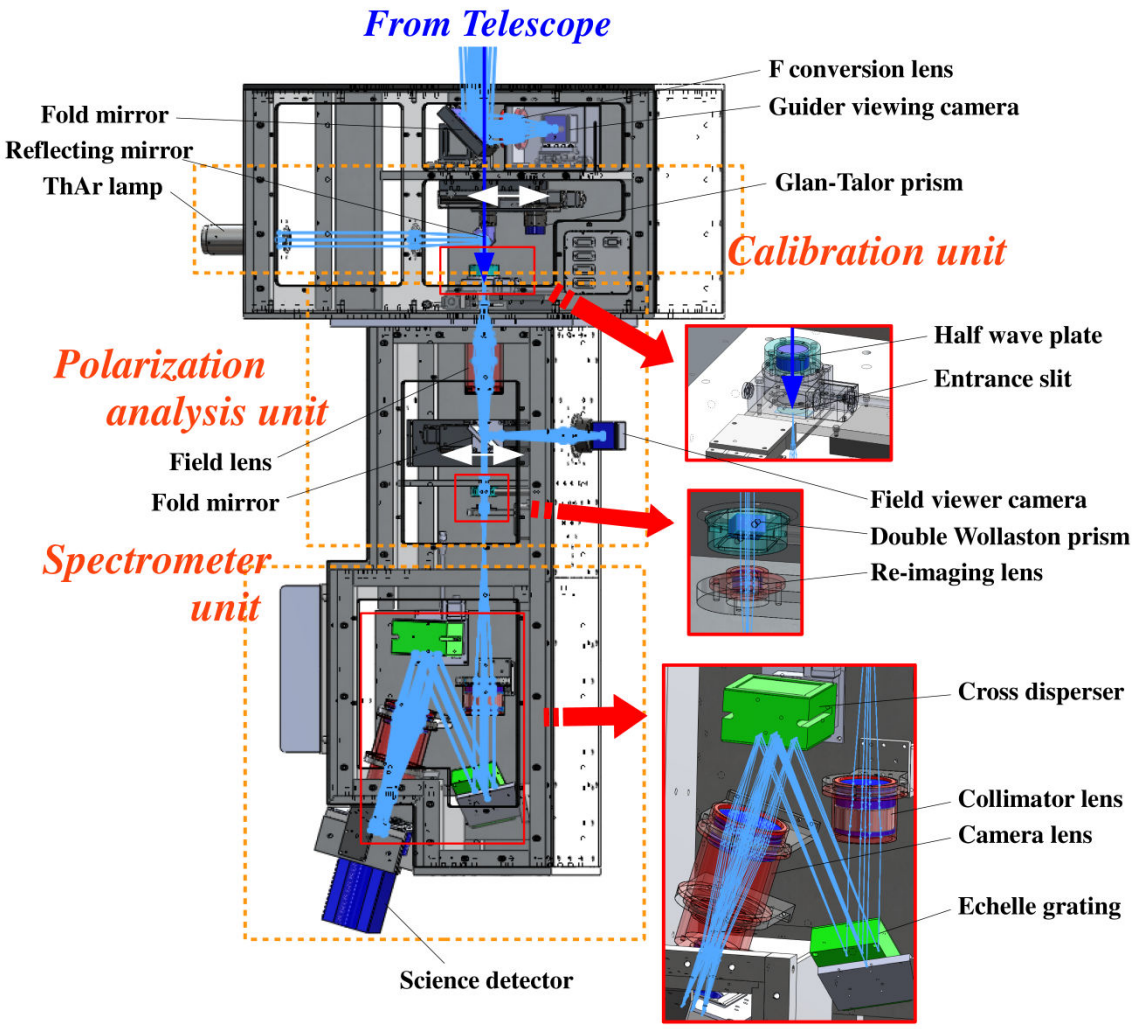

Figure 2.1 Overview of the optical layout of VESPolA

	Components	Items	Specification	Remarks
Calibration unit	Calibration lamp		Th-Ar hollow cathode	
	Glan-Talor prism	Material	Quarts	
		Depolarization	$< 5 \times 10^{-5}$	
Polarization analysis unit	Half-wave plate	Type	APSAW	See Ikeda *et al*. (2003)
		Retardance	180°	
		Retardance error	< 4° (λ = 400–800 nm)	
		Clear aperture	φ = 22 mm	
		Thickness	7.7 mm	
		Material	PMMA	
	Entrance slit	Slit length	11.8”	
		Slit width	1.5”	
	Field lens	Material	Alumina	
		Effective focal length	84.4 mm	Seven lens elements
		Clear aperture	φ = 22 mm	
	Order sort filter	Cut-on wavelength	< 445 nm (95% cut-on)	
		Clear aperture	φ = 34.7 mm	
		Thickness	3 mm	
		Material	L40	L40 (OMG. Co. LTD)
	Analyzer	Type	Double Wollaston prism	
		Material	Quartz	
		Separation angle	~0.6° at 661.7 nm	
	Re-imaging lens	Effective focal length	65.3 mm	Three lens elements
		Clear aperture	φ = 15 mm	
Spectrometer unit	Collimator lens	Effective focal length	300 mm	Three lens elements
		Clear aperture	φ = 62 mm	
	Echelle grating	Blaze angle	44°	
		Groove density	72 mm^{-1}	
		Clear aperture	95 × 62 mm	
	Cross disperser 1	Blaze wavelength	760 nm	For red wavelength
		Groove density	300 mm^{-1}	
		Clear aperture	85 × 85 mm	
	Cross disperser 2	Blaze wavelength	500 nm	For blue wavelength
		Groove density	600 mm^{-1}	
		Clear aperture	85 mm × 85 mm	
	Camera lens	Effective focal length	300 mm	Five lens elements
		Clear aperture	φ = 80 mm	
Detector		Type	Front illuminated	E2V CCD42-40
		Pixel format	2048 × 2048	
		Pixel size	13.5 µm x 13.5µm	
		Read-out noise	2.97 [e^-]	
		Gain	1.79 [e^-/ADU]	
		Dark current	0.6×10^{-4} [e^-/sec] at 183 K	

Table 2.2 Basic parameters of the main optical components used in VESPolA and of the related elements.

2.2.1. Polarization analysis unit

The optical layout of the polarization analysis unit is shown in Figure 2.2. It consists of only transmissive optical elements, with no mirrors. These elements are aligned along the optical axis of the telescope to minimize the instrumental polarization. The *f*/10 beam from the telescope passes through the rotatable modulator which was installed just before the polarization analysis unit. The beam is then focused on the alumina (Al_2O_3) entrance slit, which has 1.5" width and 11.8" length. This alumina slit was used to prevent instrumental polarization at the edges of slit because alumina is a dielectric (Ikeda *et al*. 2003). We used a non-ripple super-achromatic half-wave plate as the modulator, and the effective clear aperture is 22 mm. Because this wave-plate consists of five PMMA layers (n = 1.49) and adhesive (n = 1.51) between these layers, the internal reflections and resulting ripple in the polarization spectra are minimized. After the light passed through the entrance slit, it is collimated by the field lens unit (F_{fie} = 84.4 mm), which consisted of seven lenses and produced a pupil image with a diameter of 8.45mm located 318.7 mm from the entrance slit. At the rear of the field lens unit, an order-sort filter is located to eliminate the second-order diffracted light generated by the red-cross disperser (see section 2.2.2). This lens unit is also significant in the fore optics of the field viewer system, which is described in the following section. The Lyot stop is located at the of the exit pupil to block stray light. The diameter is 8.4 mm, which is slightly smaller than the original pupil diameter (8.45 mm). A double Wollaston prism analyzer is installed after the Lyot stop consisting of three quartz prisms, and the separation angle is 0.6° at 661.7 nm. The double Wollaston prism splits the modulated light into two orthogonal polarized rays (o- and e-ray). The two

polarized images are reproduced at the objective plane of the spectrometer by the re-imaging lens unit (F_{rei} = 65.3 mm), which consisted of three lenses. The magnification factor between the telescope focal plane image and reproduced images was F_{rei}/F_{fie} = 0.77.

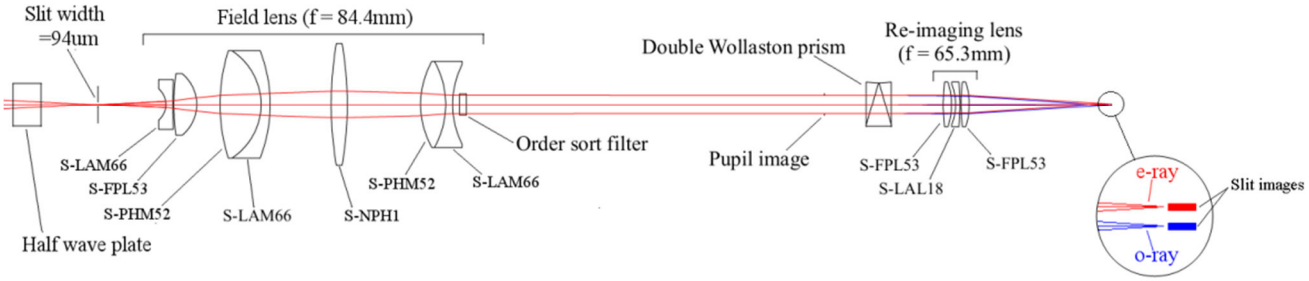

Figure 2.2 Optical layout of the polarization analysis unit.

2.2.2. Spectrometer unit

The optical layout of the spectrometer unit is shown in Figure 2.3. The optical configuration is optimized so that the occupied volume of the unit was minimized without the vignetting. The o- and e-images separated by a Wollaston prism are collimated using an f = 300 mm lens unit consisting of three lenses and dispersed using an echelle grating (Newport Corporation, USA) located at the exit pupil of the collimator lens unit. The groove density of the echelle grating is 72 mm^{-1}, and the blaze angle is 44º. The grating equation is given by

$$m\lambda = d(sin\alpha + sin\beta)cos\gamma \qquad (2.1)$$

where m is the diffraction order, d is the groove spacing, α is the angle of incidence of the light, β is the dispersion angle, and γ is the angle between the incident light and the diffraction surface (Schroeder 2000). VESPolA employs a quasi-Littrow configuration (i.e., $\alpha = \beta$) with $\gamma = 12°$. The diffracted light from the echelle grating is incident on the cross dispersers of the reflective gratings. There were two cross dispersers. One has a blaze wavelength of 500 nm and a groove density of 600 mm^{-1}, and it is used for the blue spectral region; the other has a blaze wavelength of 760 nm and a groove density of 300 mm^{-1}, and it is used for the red spectral region. Both were sourced from Newport Corporation. They were installed in cells that were arranged back to back, and the cells were located on a rotation stage so that either could be selected by rotating the stage. The spectra were separated into different orders and focused to form an echellogram on the detector using the camera lens unit (f = 300 mm), which consisted of five lenses. The camera was a commercially available cooled CCD array unit (850 series, Spectral Instruments Inc., US) and employed a front-illuminated 2K x 2K array (CCD42-40, E2V

Technologies, UK). A pixel size is 13.5 × 13.5 μm. The array is cooled to 183 K, and controlled within ±0.1 K using a thermoelectric cooler (TEC) together with a water cooling system. The dark current is suppressed to less than 0.001 e^-/pixel/s. The read-out noise is 2.97 e^- under the conditions for the conversion factor of 1.79 e^-/ADU and the read-out speed of 100 kHz/pixel. The monochromatic slit image size is 5.4 × 42.3 pixels (72.6 × 570.8 μm) at the detector, which is equivalent to a magnification factor of $\beta = 0.77$ for the whole optical system. The final spectral resolution at the center wavelength of each order is R_c = 7,972 (in the paraxial approximation). Because we have a plan to introduce a higher resolution mode of R = 20,000 in the future (see Arasaki *et al*. 2014), the slit width of R = 8,000 mode is over-sampled at 5.36 pixels/slit width.

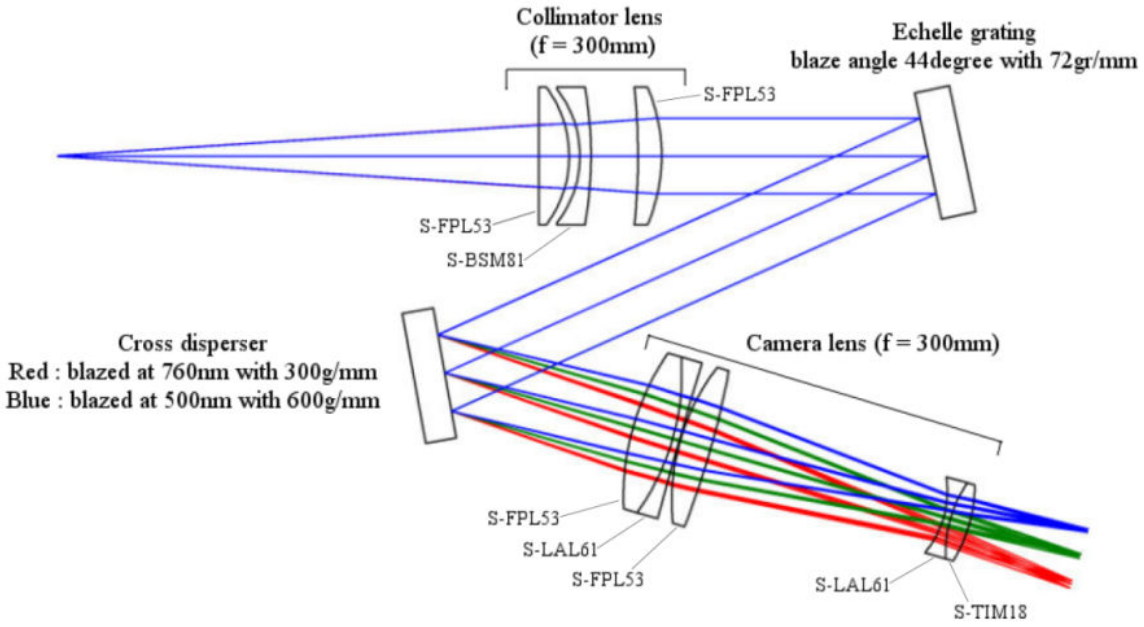

Figure 2.3 Optical layout of the spectrometer unit.

A simulated echellogram at the detector is shown in Figure 2.4. The polarized o- and e-spectra of same order are aligned side by side, and the minimum separation of the o- and e-spectra is 10 pixels (the separation is slightly different depending on wavelengths mainly due to the chromatic effect of the double Wollaston prism). The smallest separation of spectral images is 17 pixels between the o-spectrum with m = 35 and the e-spectrum with m = 34. VESPolA covers a wavelength range of $\delta\lambda \sim 250$ nm (i.e., 550–800 nm) with $23 \leq m \leq 35$ using the red cross-disperser and $\delta\lambda \sim 150$ nm (i.e., 400–550 nm) with $36 \leq m \leq 48$ using the blue cross-disperser with a single exposure. Figure 2.5 shows spot diagrams at various positions (i.e., various wavelengths) at the detector. The geometrical root mean square (rms) diameters were within an area of 2 × 2 pixels (i.e., 27 × 27 μm) at all wavelengths.

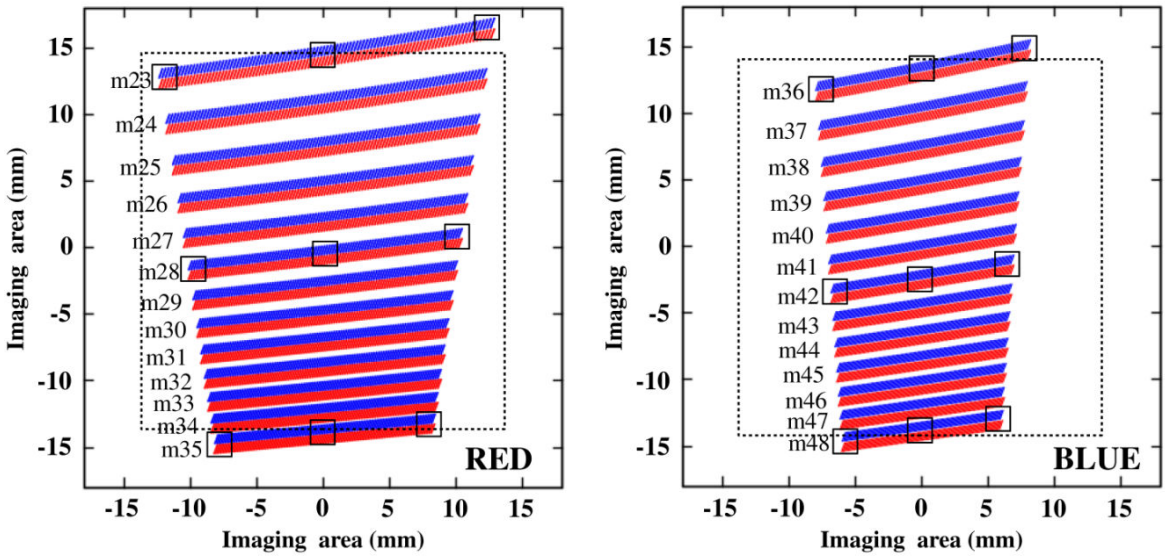

Figure 2.4 Simulated echellograms of the red spectral region ($23 \leq m \leq 35$) (left) and the blue spectral region ($36 \leq m \leq 48$) (right). The blue lines show the o-rays, and the red lines show the e-rays. The dashed squares correspond to the size of the detector. The spot diagrams shown in Figure 5 are evaluated at the wavelengths shown in the small squares.

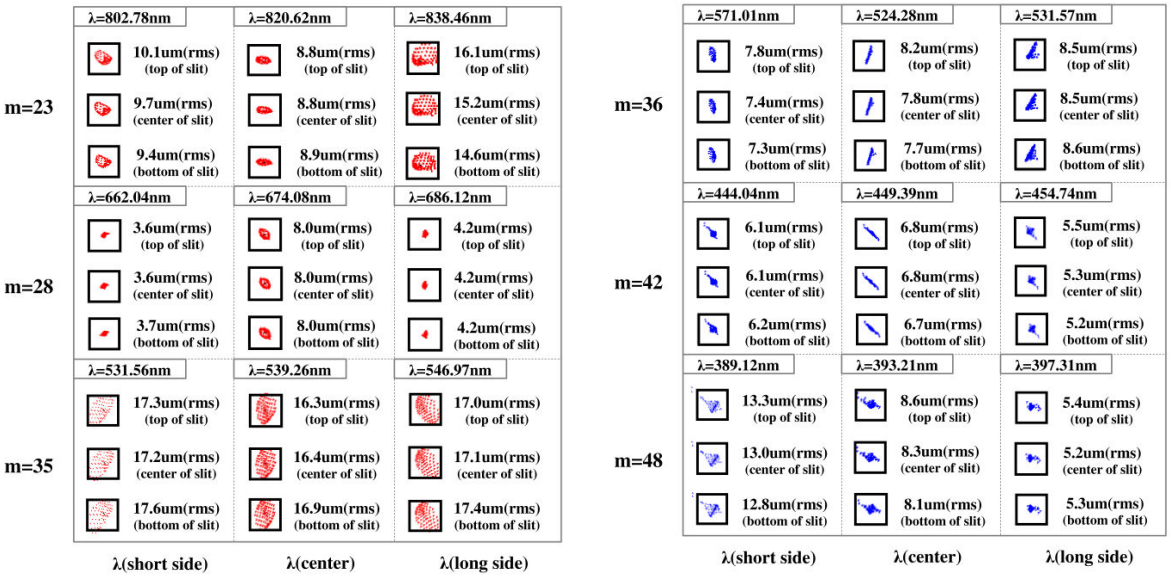

Figure 2.5 Spot diagrams at various positions at the detector (i.e., at various wavelengths). The small boxes are equivalent to a size of 2 × 2 pixels (27 × 27 μm). The upper, the center, and the lower boxes for each wavelength show the upper end, center, and lower end of the slit, respectively.

2.2.3. Field viewer

VESPolA has a field viewer to place the target star onto the slit, which is used to observe the star and the surrounding field of view. Figure 2.6 shows the optical layout of the field viewer, which was installed at the rear of the entrance slit. Spectrometers often employ a tilted slit mirror made of a polished metal, which reconstructs the focal plane image of the telescope by refocusing the stellar light reflected by the slit mirror. VESPolA does not use a metallized slit mirror, and instead uses a dielectric slit (made of alumina). This is because a metalized slit may generate significant polarization at the edges (Ikeda *et al*. 2003). Because the alumina slit cannot function as a mirror, VESPolA uses a rear-type field viewer. This field viewer consisted of the field lens unit, a fold mirror, and a doublet lens. The light passing through the focal plane is collimated by the field lens in the polarization analysis unit and then reflected to the right from the path of the science camera via the fold mirror. The reflected light is focused onto the CCD array camera by the doublet lens (f = 125 mm). The CCD camera is a DMK41AU02.AS developed by Imaging Source, Inc., Japan. The format was 1280 × 960 pixels, and the pixel size was 4.65 × 4.65 μm. This camera covers a field of view of 1.5’ × 1.9’. We can see the entire of the field of view by removing the entrance slit, which is mounted on a linear stepper motor stage (SURUGA-SEIKI Ltd., Japan) (see section 2.3 for further details). The repeatability of the positioning at the entrance slit of the stage is ±0.5 μm (±0.008”), which is negligible compared with the accuracy of the wavelength calibration.

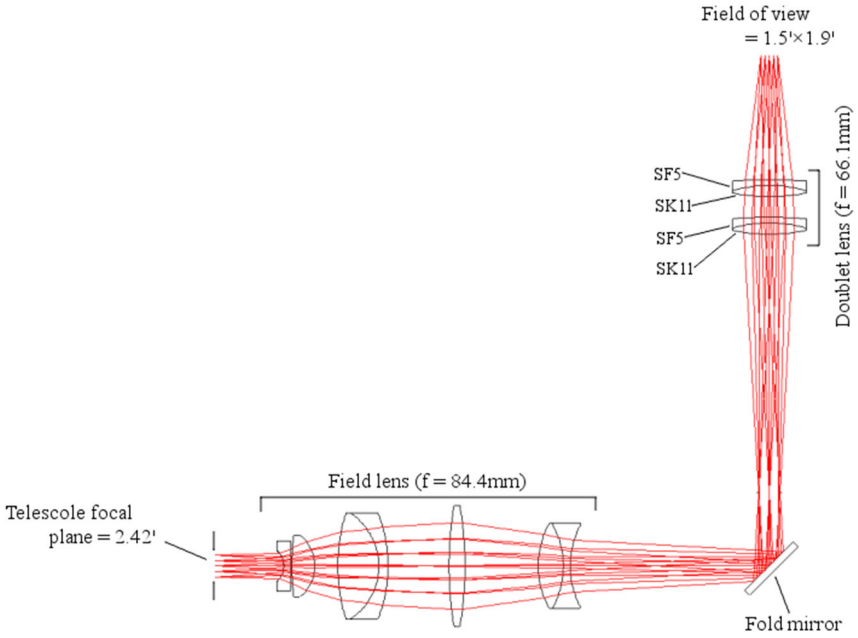

Figure 2.6 Optical layout of the field viewer.

2.2.4. Auto guider

VESPolA is equipped with an auto guider in the calibration unit. The optical layout is shown in Figure 2.7. A 45º fold mirror and an achromatic reducer lens (*f*/10 → *f*/3) produce a large field of 4.1' × 5.4' on the CCD camera (see section 2.2.2 for details of the CCD array camera). The center of the field is shifted from the telescope optical axis by 11.3' (see Figure 2.7), which results in a large coma aberration over the field of view due to the fact that the Araki-telescope is a classical Cassegrain telescope (Schroeder 2000). To correct for this aberration, we added a doublet lens with a displacement of 2.5 mm from the optical axis of the reducer lens. Figure 2.8 shows the final spot diagrams of the auto guider optics together with a photographic image. All the spots fall within 2", which is less than the typical seeing at the Koyama Astronomical Observatory site. The limiting magnitude was m_v = 15.5 mag to achieve a signal-to-noise ratio of S/N > 10 with an integration time of 10 s. According to the Guide Star Catalog II (Lasker *et al*. 2008), it should always be possible to select a guide star form at least 13 guide stars that are brighter than m_v = 15.5 mag in a field of 4.1' × 5.4'.

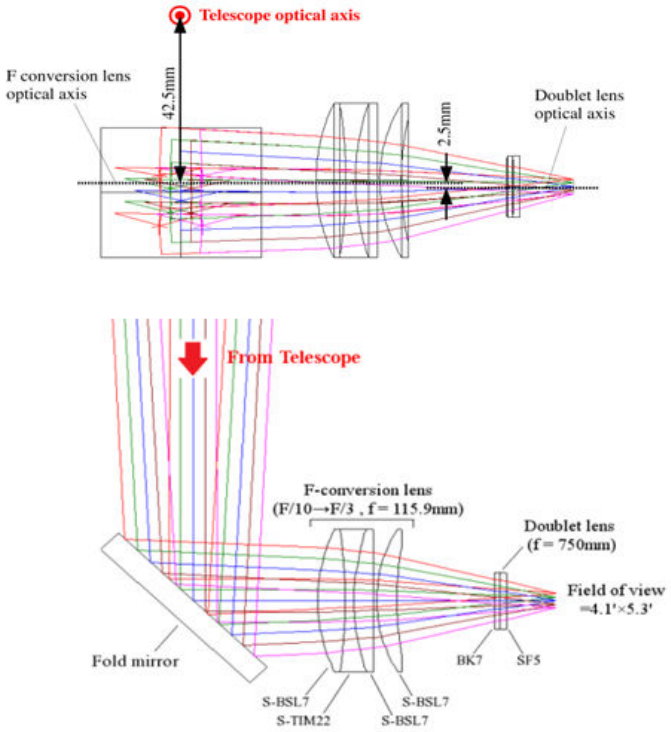

Figure 2.7 Optical layout of the auto guider. The upper images show a top view, and the lower show a side view.

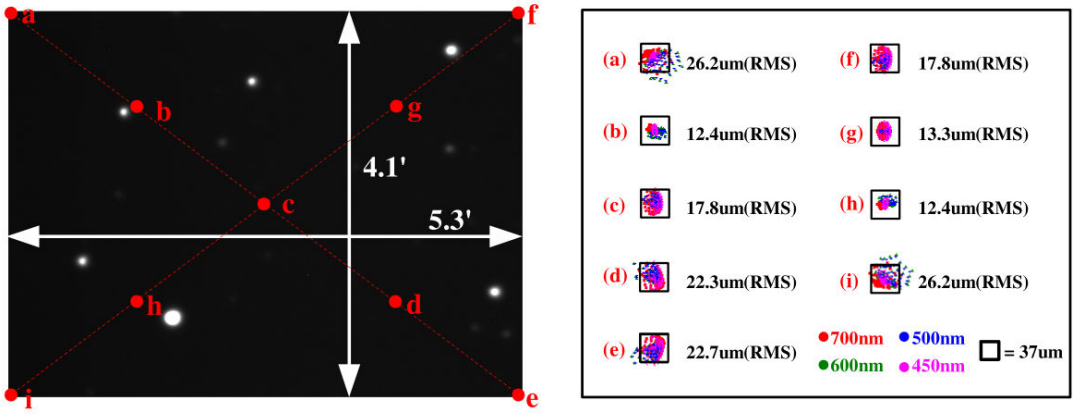

Figure 2.8 A photographic image (left) and spot diagrams (right) by the auto guider. The alphabetized labeling represents the locations shown in the FOV photograph. The box size was 2 × 2 pixels (37 × 37 μm). The red, green, blue, and pink plots correspond to wavelengths of 700 nm, 600 nm, 500 nm, and 450 nm, respectively.

2.3 Control system

VESPolA has two rotary stages and three linear stages, motorized using five-phase stepper motors to switch between optical elements (see Figure 2.9 and Table 2.3). The rotary stages are equipped with a calibration unit to rotate the wave plate and to switch between cross dispersers in the spectrometer unit. The linear stages are used (i) in the calibration unit to insert a calibration optical system, such as a polarization prism and a fold mirror to introduce the light from a calibration lamp, (ii) at the top of polarization analysis unit, to switch slits, or (iii) in the polarization analysis unit, to insert a fold mirror for the field viewer. All stages are sourced from SURUGA-SEKI, Ltd., Japan, and could be controlled remotely using two-axis controllers via USB cables using a PC located in the dome running Microsoft Windows XP (see Figure 2.9). To achieve the polarimetric accuracy of $\delta P \sim 0.1\%$, the positional accuracy of the rotary stage for the wave plate should be less than ±0.1° (Ikeda *et al*. 2004). The used rotary stage (SURUGA-SEKI KXC0620) has a repeatability of ±0.01° in rotation.

The HCT-lamp used for wavelength calibration is switched with a custom-built relay circuit attached to a port of a stage controller. This remote actuation system was operated using the VESPolA Command line interface (VESPolA-Colin), which is a command prompt program on Windows XP, written in C++. The three CCD cameras (i.e., the field viewer camera, auto guider camera, and science camera) were controlled using USB 2.0 connections from the PC. During the observations, the PC was remotely controlled via a LAN using a remote desktop application from a Linux PC in the control room adjacent to the observation dome.

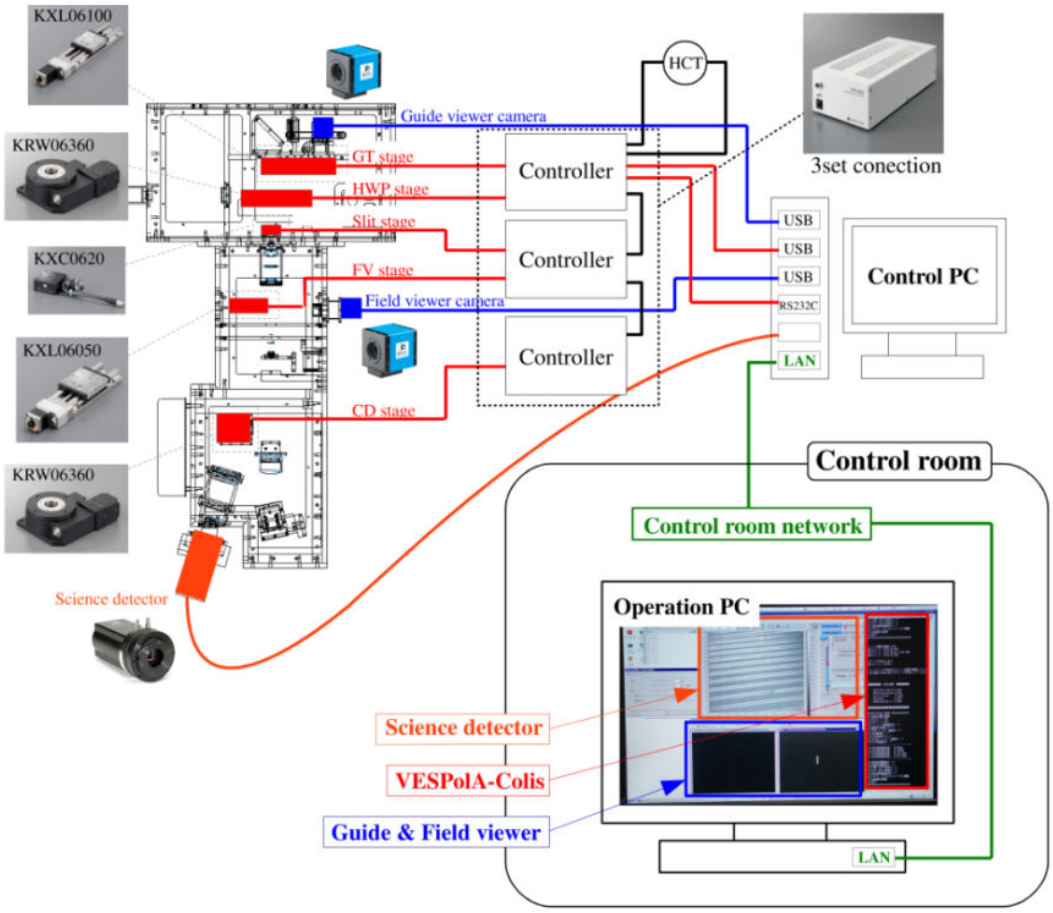

Figure 2.9 Schematic layout of VESPolA control system.

Name	Model number	Slide stroke	Repeatability	Function
GT stage	KXL06100	100 mm	±0.5 μm	Introducing the calibration lamp or inserting a GT prism
HWP stage	KRW06360	360°	±0.01°	Rotating wave plate
Slit stage	KXC0620	20 mm	±0.5μm	Switching slits
FV stage	KXL06050	50 mm	±0.5μm	Inserting a fold mirror for the field viewer
CD stage	KRW06360	360°	±0.01°	Selecting cross dispersers

Table 2.3 Specifications of the motorized stages used in VESPolA.

3. Data reduction procedure

We obtained linear polarization spectra, *Q/I(λ)* and *U/I(λ)*, from four pairs of o- and e-spectra taken at different angles of the HWP, i.e., $\psi = 0°$, $\psi = 45°$, $\psi = 22°.5$, and $\psi = 67°.5$ (Kawabata *et al*. 1999). This method, termed the "four-angles method", enables highly accurate polarimetry because it can correct for time variations in the brightness of the target star under unstable weather conditions, and for an efficiency difference between the o- and e-rays in the optical system without additional calibration spectra. We used a data reduction procedure for the polarization spectra described in the following subsections.

3.1. Data set for calibration

We divided the reduction procedure into two parts: spectroscopy reduction and polarization calibration. We use object images, dark images, flat images, and comparison lamp images to obtain one-dimensional o- and e-spectra in the former. We use images of various standard stars, including an unpolarized (UP) star, a strongly polarized (SP) star, and a totally polarized stellar image obtained using a Glan–Taylor (GT) prism to obtain the final Stokes spectra *Q/I(λ)* and *U/I(λ)*. We selected these standard stars from Serkowski (1974), Schmidt *et al*. (1992), and Wolff *et al*. (1996).

3.2. Data reduction

We use IRAF in most of the data reduction steps. IRAF is distributed by the National Optical Astronomy Observatories, which are operated by the Association of Universities for Research in Astronomy, Inc., under a cooperative agreement with the National Science Foundation; http://iraf.noao.edu/.

3.2.1. Spectroscopy reduction

3.2.1.1. Dark subtraction

The operating temperature of the science camera is 183 K. Because the temperature is controlled within ±0.1 K over a single night, variations in the dark current are very small and can be neglected. Therefore, we take dark frames at the end of the night. We use 20 dark frames with the same integration times as the object frames. On a given night, we produced a median image using these 20 dark images and then subtracted this from the object frames.

3.2.1.2. Flat-fielding

We produce a flat-fielding frame using dome-flat images. The dome screen is located on the wall of the dome, which is irradiated using seven halogen lamps attached to the top ring of the telescope (Yoshikawa *et al*. 2012). We obtain three flat-field images for four different positions, i.e., HWP angles of 0°, 22°.5, 45°, and 67°.5, giving a total of twelve flat images, which are taken before or after each observation. These twelve frames are averaged

and normalized as a flat-field image, and the typical photometric error is less than 0.07% per pixel. The final polarimetric error from the flat-fielding procedure is therefore negligible.

Flat fielding simultaneously corrects for non-uniformities of the transmittance/reflectance of the optical elements, pixel-to-pixel sensitivity differences of the CCD, and fringing patterns appearing on the detector, which are generated interferometric effects in the silicon wafer. The dome screen is fixed on the wall of the dome with the elevation angle of 40°. If an object with a different elevation is observed from the dome screen, the resulting echellogram is slightly misaligned at the detector compared with that of flat-fielding frame due to bending of the instrument body. This may result in an offset of the stellar spectral order away from the flat field orders. This sometimes results in a pixel that detects the stellar image, which was not illuminated by the flat field. To minimize these effects, we adjust the stellar image to the center of the slit on the dome flat image.

3.2.1.3. Removal of cosmic rays signal

Unexpected signals from cosmic rays are removed using the *crmedian* in IRAF. For emission-line stars, we should carefully select appropriate parameters to avoid misidentifying an emission line as a cosmic ray signal.

3.2.1.4. Extraction of spectral images

We extracted two-dimensional spectral images of o- and e-ray from the echellogram image using the *apall* in IRAF. The aperture size along the slit length is determined as a full width at 10% of maximal intensity for each

wavelength. For this reason, the width varied from 20 pixels to 24 pixels (5.6–6.7") depending on the seeing size on a given night. The extracted flux includes approximately 90% of the total detected flux. We used a fifth-order Legendre polynomial to locate the peaks of the spectra.

3.2.1.5. Wavelength calibration and distortion correction

We prepare two-dimensional spectra of Th-Ar lamp images obtained in the same manner as the object frames for wavelength calibration. We then obtain pixel–wavelength relations at the center of the extracted two-dimensional spectra using the *identify* in IRAF. A fifth-order Legendre polynomial is used as the regression function. Because the echelle grating of VESPolA is located in the quasi-Littrow configuration with $\gamma = 12°$, the monochromatic slit image not only is tilted in the dispersion direction but also form a curved shape (see Figure 2.4). To convert this distorted spectrum into a complete rectangular spectrum (so that the dispersion axis and the spatial axis are perpendicular), we use the *reidentify* and the *fitcoords* in IRAF. The *reidentify* automatically obtains a pixel–wavelength relation at a given spatial position in the slit (apart from the center of the spectra) based on the results of the *identify*. The *fitcoods* obtains a two-dimensional fitting function, which describes the relationship between the wavelength axis and the slit axis using the results of the *reidentify*. The *transform* in IRAF is used to provide rectangle spectra using the results of the *fitcoods*. The wavelength accuracy of the final spectra is better than ± 0.06 Å in all wavelengths region.

3.2.1.6. Extraction of one-dimensional spectra

We obtain one-dimensional o- and e-spectra at a position angle ψ of the HWP, resulting in the following intensities using the averaged transformed spectra along the spatial direction:

$$I_o(\lambda,\psi) = \frac{\mathrm{I}(\lambda)}{2}\left[1 + \frac{Q}{I(\lambda)}cos4\psi + \frac{U}{I(\lambda)}sin4\psi\right]S_o(\lambda)T(\lambda,\psi) \qquad (3.1)$$

and

$$I_e(\lambda,\psi) = \frac{\mathrm{I}(\lambda)}{2}\left[1 - \frac{Q}{I(\lambda)}cos4\psi - \frac{U}{I(\lambda)}sin4\psi\right]S_e(\lambda)T(\lambda,\psi) \qquad (3.2)$$

where S_o, S_e, and T are the instrumental response functions for o- and e- rays, and the time variation response function, respectively.

3.2.2. Polarization calibration

During polarization calibration, we derive the Stokes spectra $(Q/I(\lambda))_{ins}$ and $(U/I(\lambda))_{ins}$ in the celestial coordinate system using the one-dimensional spectra obtained in the previous subsection.

First, the Stokes spectra $(Q/I(\lambda))'_{ins}$ and $(U/I(\lambda))'_{ins}$ in the instrumental coordinates are obtained using the eight spectra $I_o(\lambda, 0°)$, $I_o(\lambda, 22°.5)$, $I_o(\lambda, 45°)$, $I_o(\lambda, 67°.5)$, $I_e(\lambda, 0°)$, $I_e(\lambda, 22°.5)$, $I_e(\lambda, 45°)$, and $I_e(\lambda, 67°.5)$, as described in Kawabata *et al*. (1999), so that we obtain Stokes spectra in which $S_o(\lambda)$, $S_e(\lambda)$, and $T(\lambda, \psi)$ are eliminated. Second, we subtract a component of the instrumental polarization determined with $(\mathrm{Q/I}(\lambda))_{UP}$ and $(U/I(\lambda))_{UP}$ from the object Stokes spectra of $(Q/I(\lambda))'_{ins}$ and $(U/I(\lambda))'_{ins}$, i.e.,

$$(Q/I(\lambda))''_{ins} = (Q/I(\lambda))'_{ins} - \left(\frac{Q}{I(\lambda)}\right)_{UP} \qquad (3.3a)$$

and

$$(U/I(\lambda))''_{ins} = (U/I(\lambda))'_{ins} - \left(\frac{U}{I(\lambda)}\right)_{UP} \qquad (3.3b)$$

Third, we correct for instrumental depolarization effects with a depolarization factor $\gamma(\lambda)$, obtained from fully-polarized GT spectra, i.e.,

$$(Q/I(\lambda))'''_{ins} = \left(\frac{Q}{I(\lambda)}\right)''_{ins} / \gamma(\lambda) \qquad (3.4a)$$

and

$$(U/I(\lambda))'''_{ins} = \left(\frac{U}{I(\lambda)}\right)''_{ins} / \gamma(\lambda) \qquad (3.4b)$$

Finally, we obtain the converted Stokes spectra in the celestial coordinate system, with the difference in the position angle between the celestial and instrumental coordinate systems, $\delta\theta_{ins}(\lambda)$, which was obtained from

the SP spectra and the GT spectra, i.e.,

$$(Q/I(\lambda))_{ins} = cos(2\delta\theta_{ins}(\lambda)) \cdot (Q/I(\lambda))'''_{ins} - sin\big(2\delta\theta_{ins}(\lambda)\big) \cdot (U/I(\lambda))'''_{ins} \qquad (3.5a)$$

and

$$(U/I(\lambda))_{ins} = sin(2\delta\theta_{ins}(\lambda)) \cdot (Q/I(\lambda))'''_{ins} + cos(2\delta\theta_{ins}(\lambda)) \cdot (U/I\,(\lambda))'''_{ins} \qquad (3.5b)$$

4. Performances of VESPolA

We carried out observations to evaluate the performance of VESPolA over 29 nights from November 2012 to November 2013. We observed several polarization standard stars, UPs and SPs, and a spectroscopic standard (SS) star. Polarization standard stars, UPs and SPs, were used to evaluate the polarimetric accuracy, and SSs were used to estimate the optical throughout. Additionally, we used a Th-Ar lamp spectrum to evaluate the spectral resolution. The observational logs are summarized in Table 4.1.

Object type	Object name	Spectral type	m_v	P_v	Date	JD	Integration time
UPs	HD47105	A0IV	1.93	0.0022	2012 Nov 27	2456259.2	60s×4
					2012 Nov 28	2456260.2	60s×4
					2012 Nov 29	2456261.3	60s×4
					2012 Dec 14	2456276.2	60s×4
					2013 Jan 12	2456305.0	60s×4
					2013 Jan 18	2456311.1	60s×4
					2013 Jan 30	2456323.0	60s×4
					2013 Jan 31	2456324.0	60s×4
UPs	HD95418	A1V	2.37	0.0018	2012 Nov 27	2456259.3	60s×4
					2012 Nov 28	2456260.2	180s×4
					2012 Nov 29	2456261.3	60s×4
					2012 Dec 14	2456276.2	60s×4
UPs	HD39587	G0V	4.40	0.013%	2012 Nov 27	2456259.3	180s×4
					2012 Nov 28	2456260.3	200s×4
					2012 Nov 29	2456261.3	120s×4
					2012 Dec 14	2456276.2	180s×4
					2013 Jan 12	2456305.0	100s×4
UPs	HD61421	F5IV	0.37	0.005%	2012 Nov 29	2456261.2	30s×4
					2012 Dec 14	2456276.2	30s×4
					2013 Jan 11	2456304.1	30s×4
					2013 Jan 12	2456305.1	15s×4
					2013 Jan 18	2456311.1	30s×4
					2013 Jan 30	2456323.0	30s×4
SPs	HD198478	B3Ia	4.83	2.72%	2013 Sep 29	2456324.0	600s×4
SPs	HD21291	B9Ia	4.12	3.53%	2013 Nov 08	2456605.1	400s×4
SPs	HD25090	B0.5III	7.30	5.70%	2013 Nov 15	2456612.1	1200s×4
SPs	HD25443	B0.5III	6.74	5.17%	2013 Nov 18	2456615.1	1200s×4
SPs	HD7927	F0Ia	4.99	3.41%	2013 Nov 19	2456616.1	900s×4
SSs	HD93521	O9Vp	7.03	-	2013 Mar 11	2456363.3	180s

Table 4.1 Summary of the observed standard stars. UPs and SPs were selected from Serkowski (1974), Schmidt *et al*. (1992), and Wolff *et al*. (1996). SSs were selected from Turnshek *et al*. (1990).

4.1. Spectral resolution

Figure 4.1 shows the spectral resolution, i.e., $R = \lambda/\delta\lambda$, which was determined by measuring the full-width at half-maximum (FWHM) of emission lines seen in the spectra of the Th-Ar lamp used for wavelength calibration. The measured spectral resolutions are distributed within the range of $7{,}750 < R < 8{,}250$ throughout the entire spectral region, which well agrees with spectral resolutions calculated using the optical model of VESPolA (see section 2.2.2). We therefore conclude that VESPolA can archive the required spectral resolution.

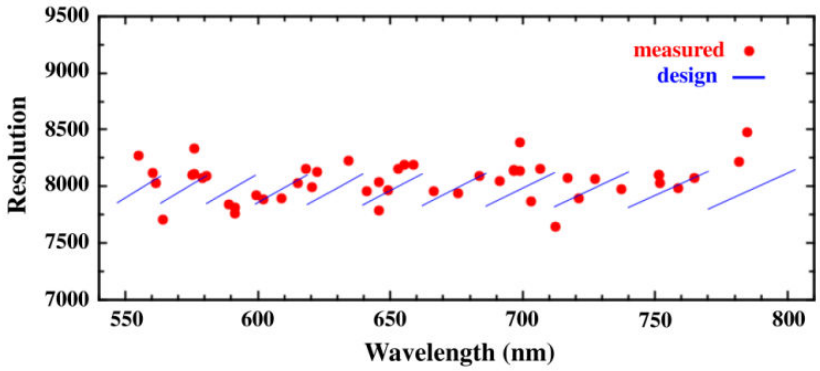

Figure 4.1 Spectral resolution of VESPolA. The filled circles show measured data using the Th-Ar lamp; the solid lines show the spectral resolutions based on the optical model of VESPolA (see section 2.2.2).

4.2. Polarimetric accuracy

If a target star has a small degree of polarization (< 1%), the polarimetric accuracy is influenced by random errors, including instabilities around the zero point of the Q–U plane. If it has a large degree of polarization, systematic errors that depend on the degree of polarization may be dominant despite corrections for the effects of depolarization. Therefore, we should evaluate the polarimetric accuracy in both cases. The former was evaluated using UP spectra, and the latter using SP spectra.

4.2.1. Polarimetric instability

Figure 4.2 shows the frequency distributions of the averaged *Q/I* and *U/I* in individual echelle orders for the 24 UPs listed in Table 5 during 3 months. The distributions exhibit a Gaussian-like profile, with a mean of approximately 0%. The standard deviations of *Q/I* and *U/I* are 0.019% and 0.017%, respectively. VESPolA therefore achieves a polarization stability of $\delta P_{st} \sim 0.019\%$.

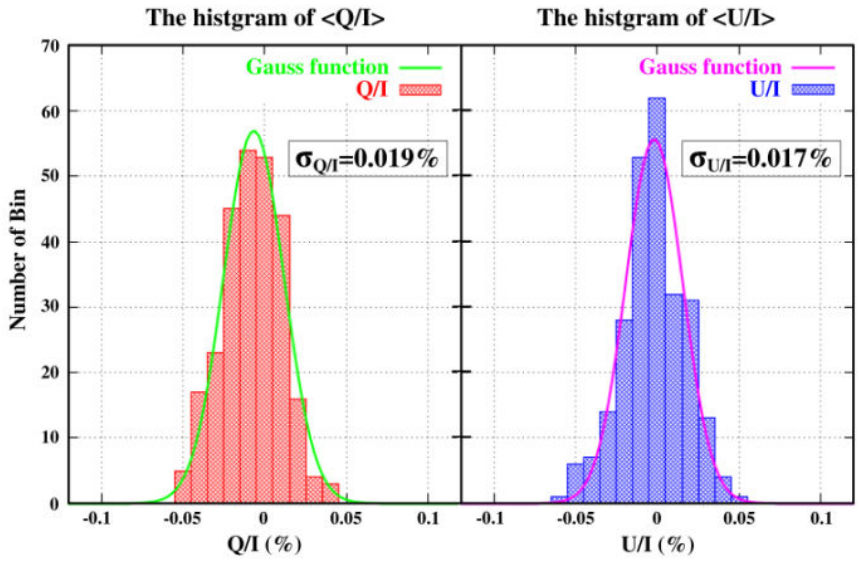

Figure 4.2 Histograms of *Q/I* and *U/I* for several unpolarized standard stars. These histograms show the averaged Stokes *Q/I* and *U/I* for the individual orders in the range $24 \leq m \leq 34$. The solid lines show the fitting to the Gaussians. The standard deviation of *Q/I* and *U/I* are 0.019% and 0.017%, respectively.

4.2.2. Polarimetric error across the line and polarization ripple

Figure 4.3 shows the intensity spectrum and the Stokes *Q/I* and *U/I* spectra of HD4715 (UP). Because telluric absorption and the system efficiency are not corrected for in this intensity spectrum, we can see broadened peaks for each order, which is attributed to the blaze function of the echelle grating. The standard deviations of the Stokes spectra are 0.05% for the entire wavelength range, but most of this scatters are inference by ripple (see the upper panel of Figure 4.3 and the following subsection).

The lower panel of Figure 4.3 shows magnified spectrum around Hα absorption line. We don't observe any anomalous polarization features, which could be produced in the reduction process, such as wavelength calibration error between the o- and e-spectra.

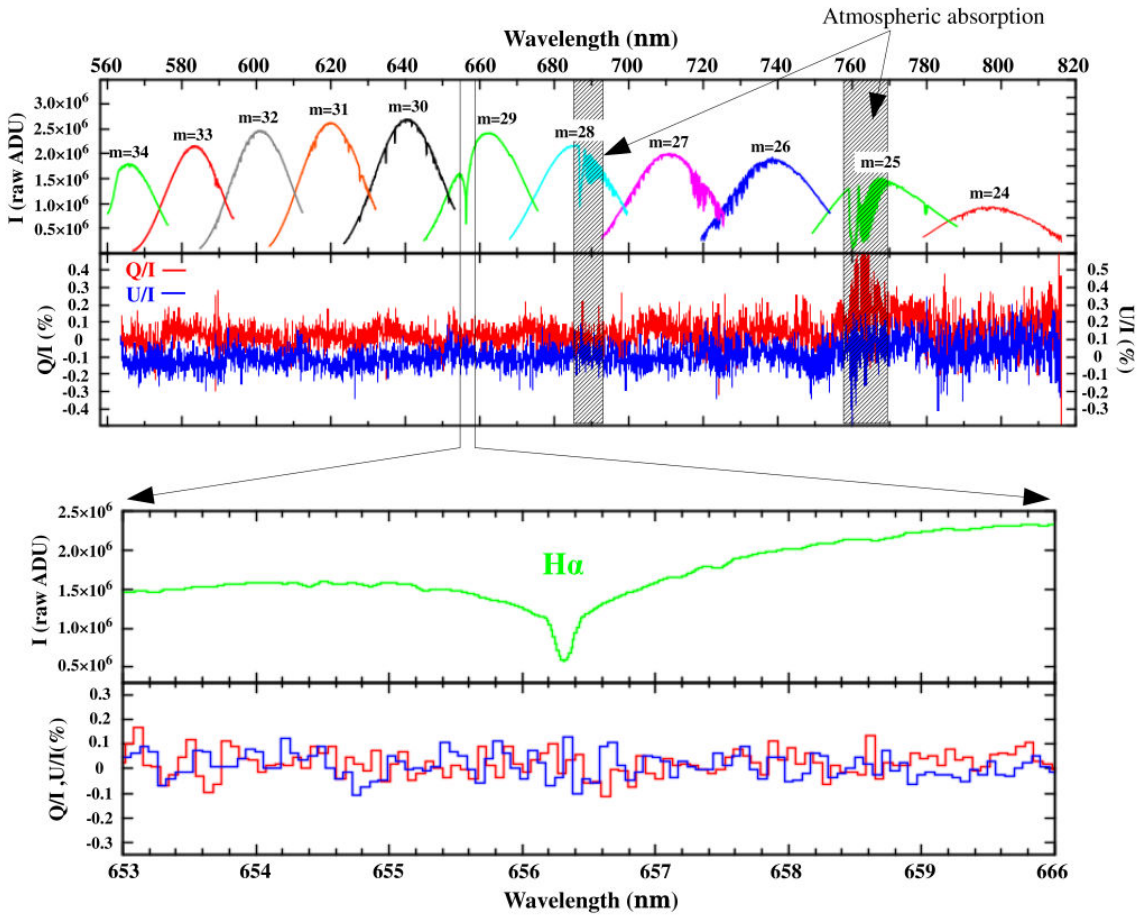

Figure 4.3 Observed spectra of HD47105 (UP). The upper panel shows the raw count of CCD (top) and Stokes *Q/I* and *U/I* spectra in the range $24 \leq m \leq 34$ (bottom). The lower panel shows close-up spectra shown in the upper panel around the Hα absorption line (653–666 nm). Anomalous patterns due to the reduction process are not observed in the polarization spectra of Hα.

4.2.3. Polarization ripple

Figure 4.4 shows a magnified image of the *Q/I* and *U/I* spectra in the range 660–670 nm to investigate the presence (or absence) of ripple, which was reported by Donati *et al*. (1999). Polarization ripple appears to be eliminated; however, a small amplitude variation with a pseudo-period of approximately 0.2 nm is seen, which is larger than the 3σ error bar determined from the photon shot noise. This small ripple is attributed to internal reflections generated at the boundaries between the PMMA layer (with a refractive index of n = 1.49) and the adhesive layer (with a refractive index of n = 1.51) due to the small differences in the refractive index. Similar results were also reported by Ikeda *et al*. (2003). The amplitude and the phase of the ripple are not stable through-out the night because of the variations in the ambient temperature. Thus, the ripple pattern should be considered random errors, and the rms magnitude is estimated to be $\delta P_{\mathrm{ripple}} \sim 0.05\%$.

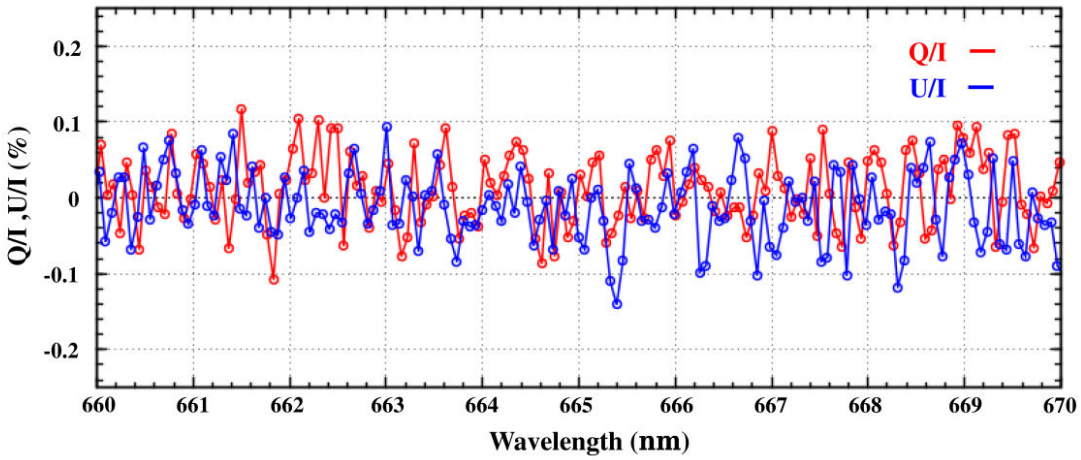

Figure 4.4 Magnified view of the *Q/I* and *U/I* spectra in the range 660–670 nm. The spectra are binned in wavelength intervals equivalent to a monochromatic slit image, i.e. the spectral resolution δλ.

4.2.4. Polarimetric error depending on polarization degree

We evaluated the dependence of the polarimetric error on the degree of polarization using the results of the five SPs listed in Table 4.1. Figure 4.5 shows the polarization spectrum for one of the SPs, HD21291, together with a Serkowski curve given by

$$p_{ser}(\lambda) = p_{max} exp\left[-K\ ln^2\left(\frac{\lambda_{max}}{\lambda}\right)\right] \qquad (4.1)$$

Where

$$K = 1.66(\lambda_{max}/1000nm) + 0.01 \qquad (4.2)$$

and $P_{\max}$ is the peak polarization at wavelength $\lambda_{\max}$ (Whittet *et al*. 1992). $P_{\max}$ and the $\lambda_{\max}$ are determined from existing photometric polarimeters (Hsu *et al*. 1982). The polarization spectrum is in good agreement with previously reported photometric polarimetry data. Furthermore, the polarization spectrum varies smoothly with wavelength and did not exhibit any high-frequency components of the polarization error. To evaluate the polarimetric error quantitatively, we plotted the difference in the polarization $<\delta P>$ averaged over the range 580–620 nm from the predicted Serkowski curve in Figure 4.6. The standard deviation of $<\delta P>$ is 0.05%, with no prominent dependence on the degree of polarization. This scattering of $<\delta P>$ appears to be larger than or comparable to the zero-point error estimated from the UP spectra (see sections 4.2.1. and 4.2.3). It is recognized that the error originates from uncertainties in determining the background lighting, such as the sky and the inter-order scattered light in the echellogram. (If there were an error of 1% in the background level from the peak intensities of the stellar spectrum, the final polarization spectrum would have a polarization error of $\delta P_{sp} \sim 0.05\%$ for an object

with a polarization degree of $P < 6\%$.)

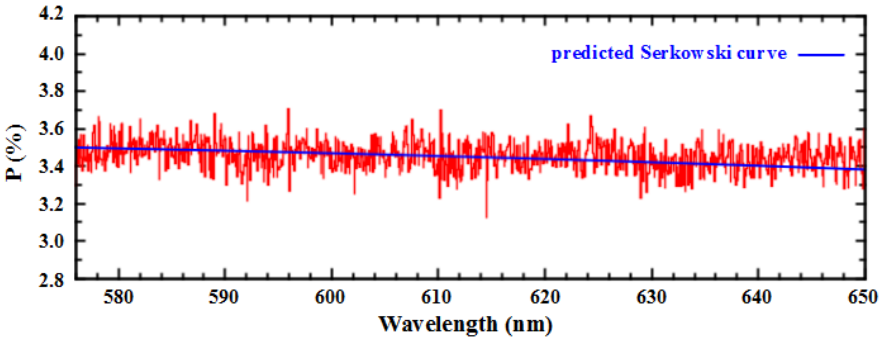

Figure 4.5 Observed polarization spectrum of an SP (HD21291). The smooth solid lines show the predicted Serkowski curve reproduced from the photometric polarimetry data reported by Hsu *et al*. (1982).

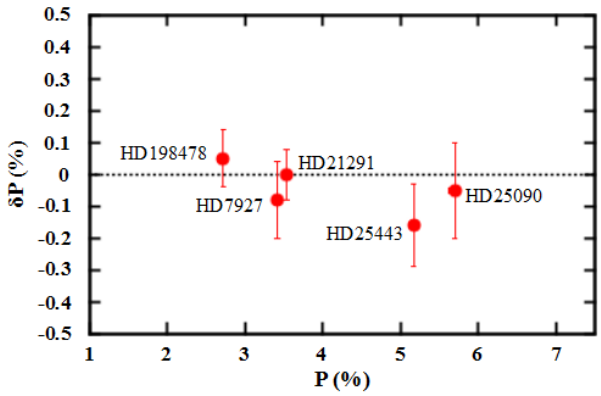

Figure 4.6 Evaluating results for polarimetric error <δ*P*> of the depolarization of five SPs. Here, <δ*P*> is the average of $\delta P = P - P_{ser}$ over the range 580–620 nm.

In summary, the polarimetric error of VESPolA is dominated by high-frequency ripple, although the amplitude of this is small. We conclude that the final polarimetric accuracy of VESPolA is $\delta P \sim 0.1\%$ with no polarization dependence for objects with $P < 6\%$, which includes the great majority of objects in astronomy.

4.3. Total throughput and limiting magnitude

Figure 4.7 shows the total optical throughput of VESPolA, which was obtained using a spectroscopic standard star, HD93521 (O9Vp). The maximum throughput is estimated to be 20.3% with m = 30, resulting in a limiting magnitude of m_v = 7.8 in the case of $\delta P < 0.1\%$, with an integration time of 4 hours, where we assumed that the atmospheric transmittance was 80% and the efficiency of the telescope was 54%. The efficiency of the telescope is estimated from the measured reflectance of the primary and secondary mirrors and the vignetting effect of the baffle cover of the secondary mirror (see Yoshikawa *et al*. 2012). The quantum efficiency of the CCD chip is determined from the specifications of the device (see http://www.specinst.com/.)

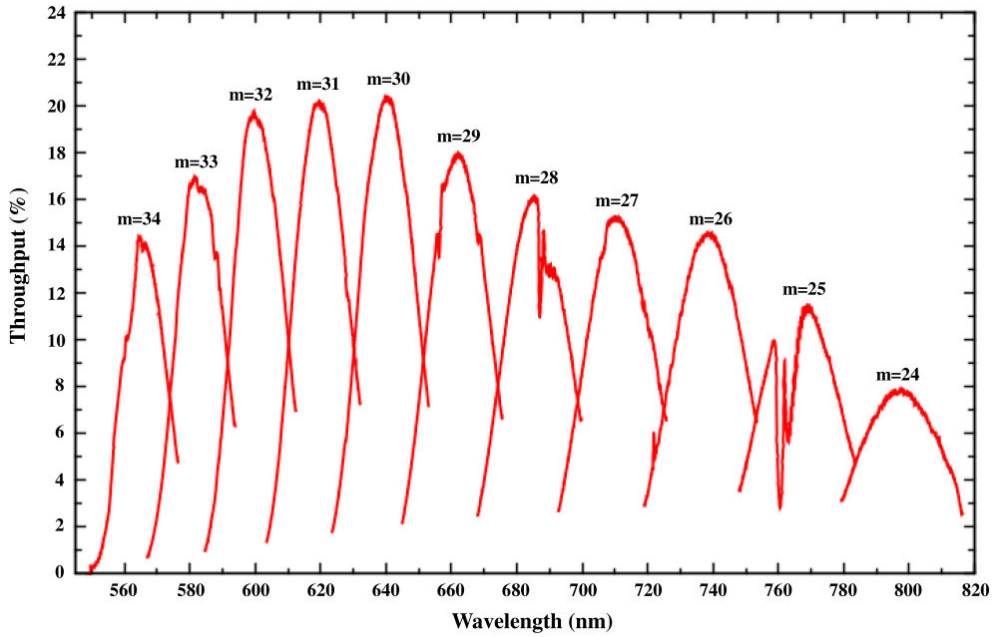

Fig 4.7. The total optical throughput of VESPolA. A maximum efficiency of 20.3% was achieved at the central wavelength for m = 30.

The overall performance of VESPolA is summarized in Table 4.2.

Items	Design	Measurement re-	Remarks
Spectral resolution	R = 7,972	R = 7,750–8,250	The central wavelength of each order
Spectral coverage	400–850 nm	400–850 nm	
Spectral coverage for single exposure	$\delta\lambda$ = 150–250 nm	$\delta\lambda$ = 150–250 nm	
Polarimetric accuracy	$\delta P < 0.1\%$	$\delta P \sim 0.1\%$	
Position angle accuracy	$\delta\theta < 1°$	$\delta\theta < 1°$	Determined by the uncertainty of position angles of SPs described in literatures
Maximum throughput	18.0%	20.3%	
Limiting magnitude	m_v = 7.7 mag	m_v = 7.8 mag	$\delta P < 0.1\%$ with the integration time of 4 hours

Table 4.2 The overall performance of VESPolA.

5. A scientific result by VESPolA - High resolution spectropolarimetry of V339 Del

5.1. Introduction

5.1.1 V339 Del

V339 Del (Nova Del 2013) is a classical nova. It was discovered by Koichi Itagaki on 2013 Aug. 14.58 (UT) with a photograph magnitude of 6.8 mag. (Waagen 2013), reached a maximum magnitude of 4.4 mag on 2013 August 16.47 (UT) (Chochol *et al*. 2014), and entered the decline phase with an order of about 1mag in a day (Figure 5.1). V339 Del was so bright that many researchers including amateur astronomers in all over the world obtained the various data in pre-maximum phase. Therefore, it becomes a very important sample for the study on the initial phase of nova passes so quickly to be still unresolved.

A couple of high resolution optical spectroscopies of this nova reported in pre-maximum phase. Munari *et al.* (2013) discovered a rapid time variation of spectral line profile on a timescale of hour and reported that it has a flat toped Hα emission line on Aug. 15.83. Shore *et al*. (2013a) and Tomov *et al*. (2013) reported that weaker metallic lines of FeII, HeI, SiII, and MgII were presented and some of them has already shown P Cygni profiles even though in the pre-maximum phase.

A lot of theoretical models on nova expansion phenomenon have been proposed so far, and succeeded to reproduce a light curve in the decline phase. Some important physical parameters of nova such as a mass of white dwarf WD and mass accretion rate from a companion can be estimated by comparing those models and photometric observations. These physical parameters obtained by these models are good agreement with those by other methods.

Recently, Hachisu & Kato (2014) proposed “a universal decline law” in the light curve of nova by scaling the light curves in decline phase with a time. This means that we can theoretically estimate the absolute magnitude of the light maximum from the optical light curve for every nova, although it has been estimated from an empirical law such as the maximum magnitude vs rate of decline (= MMRD) discussed by many researched (e.g., Downes & Duerbeck 2000). Once the absolute magnitude is previously estimated, nova could be used for one of standard candles for estimating distance in the astronomical field. Since nova is very bright (6mag < M_v < -11mag), it could give a new tool for studying the structural and dynamical. However, their theoretical model assumes a spherically symmetric expansion on nova explosion. If nova explosion is non-spherical, the estimated distance with above method is have a systematic uncertain because apparent brightness should differ between when viewed from the top and side. Actually, a bipolar jet-like structure is discovered by observations with HST in a recurrent nova RS Oph (Harman *et al*. 2008) and near infrared imaging with AO in V445 Pup (Woudt *et al*. 2009). In addition, low-resolution spectro-polarimetries indicate the existence of non-spherical geometries in a couple of novae in the early phase. Kawabata *et al*. (2001) reported that V1494 Aqr is a very fast (Pereira *et al*. 1999), show a time variation of the polarization degree and polarization angle of the continuum light from the pre-maximum phase (t = -1d) and the early decline phase (t = +8d). Ikeda *et al*. (2000) reported a difference of the polarizations between the continuum and Hα + HeII lines in a recurrent nova, U Sco (Munari *et al*. 1999), during two days from the light maximum of the outburst in 1999.

To build a model which takes the non-spherical effect into consideration and investigate the influence on the

light curve, it is essential to resolve the cause. It is impossible to resolve the geometry of nova ejecta in the early phase by the imaging except for some very close to novae. In contrast, high resolution spectro-polarimetry is a very powerful tool for this purpose, because we could obtain information on geometry and on the velocity field of each pieces in ejecta gas. However, there is few observations at present to it is still unsolved about the asymmetric cause and influence to nova. For investigate the asymmetry and those cause in explosion, to obtain the geometric structure of nova for observation is extremely important.

We carried out high resolution spectro-polarimetry of V339 Del in the early phases including pre-maximum phase. As a result, we obtained the time variation of the polarization during this observation run which would be related to the non-spherical geometry of nova. Especially, we first detected the prominent polarization of SiIIλλ6347, 6371 absorption lines in the pre-maximum stage. In this paper, we report the observation results and briefly discuss the cause of the non-spherical geometry of nova ejecta.

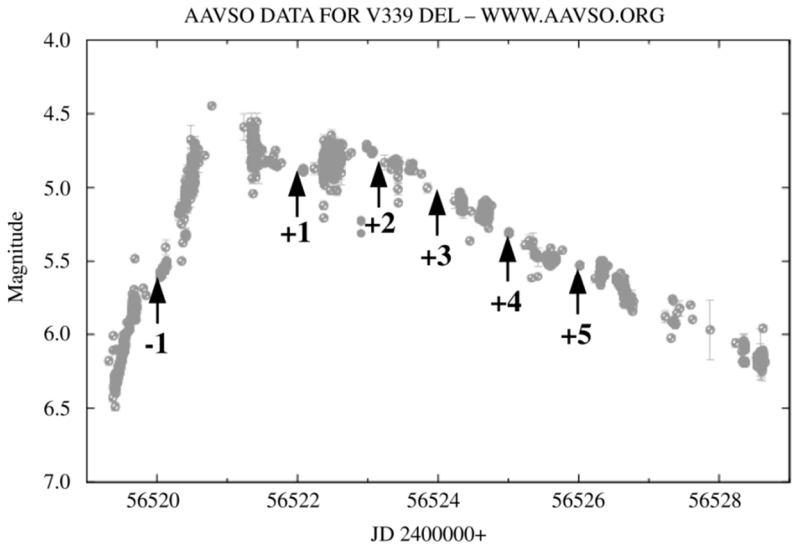

Figure 5.1 Optical light curve of V339 Del compiled from AAVSO.

The times of our observations are indicated with arrows.

5.1.2 Atmosphere structure and polarization of nova

The light emitted from a stellar photosphere has non-polarization generally because it is an incoherent sum of multiple-scattered light in the stellar atmosphere. However, in the case of electron dominated atmosphere such as an early type star, the stellar light could show a polarization at the edge of stellar disk because the polarization cannot be completely cancelled out. There is a thin atmosphere in the upper region of the photosphere because the density of the stellar atmosphere gradually decreases along the radial direction. The density graduation produces a direction bias of incident lights in the intermediate optically thick region (τ = 1 - 10), which could produce a slight polarization. Actually, Chandrasekhar (1941) predicted that the vicinity of stellar disk of an early type star could show a polarization of at most 11 % due to the electron scattering. Even if such a polarization is produced, an observed polarization from a star is approximately zero because the stellar disk perfectly forms a circle and the shape cannot be resolved spatially (The polarized lights from the edge of disk compensate the position angle another one). The polarization observed on the photosphere on the Sun whose atmosphere is not dominated by the electron scattering is not due to the scattering but the magnetic field in most cases.

Nova in the early phase has an optically thick pseudo-photosphere which is also dominated by the electron scattering. Furthermore, it is thought that optically thick nova wind forms around the pseudo-photosphere in after maximum (Hachisu & Kato 2014). Because the photosphere is geometrically thin, the continuum spectrum is dominated not by black body but the free-free emission in visible wavelength region. This means that nova photosphere shows a polarization which is produced in the atmosphere in the early type star as above mentioned. Figure 5.2 shows a

schematic illustration on the principle of generating polarization in the nova. There is a free-free emission region around the pseudo-photosphere, which is surrounded by an emission line region (actually, it should be noted that there is no physical boundary between regions because the density is gradually decreases). The polarization occurs around the outer edge of the pseudo-photosphere and the free-free emission line region by a similar mechanism as that in the stellar atmosphere. If these regions have completely spherical shapes, the polarization is not observed from the nova by totally compensating the polarization by another one.

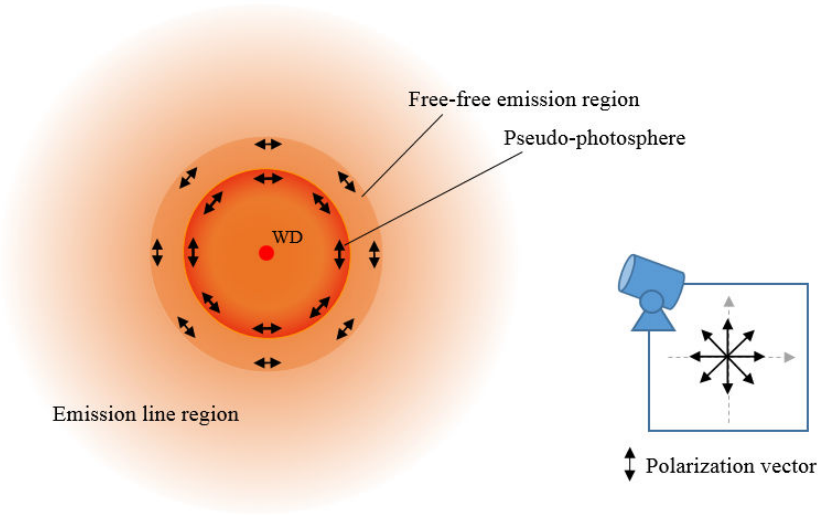

Figure 5.2 Schematic illustration of polarization in the nova.

However, if these region are asymmetrically compressed with a oblate or a prorate shape (see Figure 5.3), the polarization could be observed because the polarization generated around the outer edge of the pseudo-photosphere and the free-free emission line cannot be completely compensated due to the geometrical effect even if these cannot be resolved spatially. The geometrical thicknesses (the optical thicknesses) of these regions, that are the polarized

fluxes, are different between the equator and the pole directions. Hoflich (1991) calculates the polarization generated from the electron scattering dominated pseudo-photosphere of a supernova (= SN) with an asymmetric structure using Monte Carlo simulation. He indicates that a polarization with at most 1 % can be observed from a SN with an oblate ellipsoid photosphere of the eccentricity e = 0.6 (see Figure 5.4).

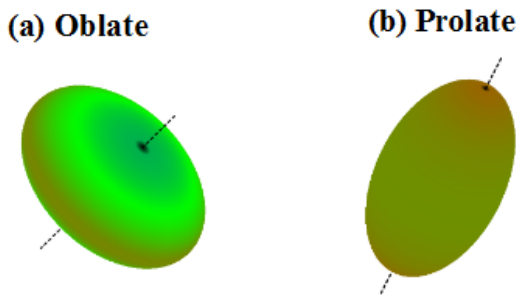

Figure 5.3 Schematic illustration of (a) Oblate and (b) Prorate ellipsoid configuration.

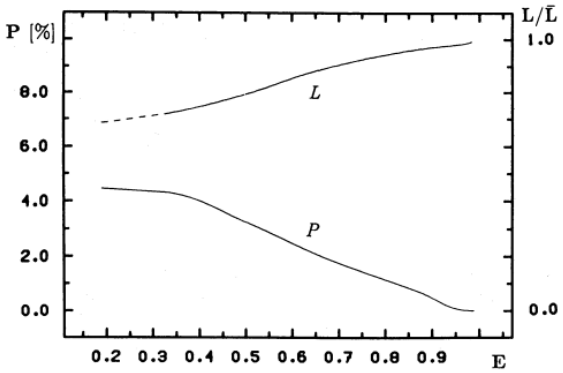

Figure 5.4 Linear polarization (P) and the normalized flux (L) as a function of the fattening E for an oblate ellipsoid (reprinted of Figure.4 of Hoflich 1991). The definition of E (= B/A) is a rate of the major axis (= A) and minor axis (= B).

5.2. Our Observation and data reduction

We observed the target (= V339 Del) at 6 nights from Aug 15 to 21 in 2013 containing the light maximum, using a high resolution spectro-polarimeter, VESPolA (Arasaki *et al*. 2014) attached to the 1.3m Araki-telescope at Koyama Astronomical Observatory of Kyoto Sangyo University (Kyoto, Japan). Table 5.1 lists the observational logs including those of several polarimetric standard stars. The observations were carried out with the "four-angles method" that takes four spectra with different angles of the HWP, i.e., $\psi = 0°$, $\psi = 45°$, $\psi = 22°.5$, and $\psi = 67°.5$ to obtain liner polarization components of Stokes spectra, *Q/I* and *U/I* (see Kawabata *et al*. 1999). For polarimetric calibration, we obtained unpolarized standard stars (HD214923 and HD432) and strong polarized standard stars (HD7927 and HD198478). Furthermore, to correct instrumental depolarization effect, we took a 100% polarized stellar (HD432's) images obtained through a Glan-Taylor prism (GT) which is located just before a slit. We reduced the images and obtained final polarization spectra with a standard reduction procedure for VESPolA (Arasaki *et al*. 2015) which mainly uses IRAF tasks.

Object name	Spectral type	JD	Integration time
V339 Del	FeII	2456520.0	300s×20
	FeII	2456522.0	300s×12
	FeII	2456523.2	100s×12
	FeII ?	2456524.0	100s×28
	He/N ?	2456525.0	100s×16
	He/N ?	2456526.0	100s×20
HD214923 (UP)	B8V	2456521.2	100s×16
		2456522.2	100s×16
		2456523.3	100s×12
		2456525.2	100s×12
HD432 (UP)	F2III	2456526.2	100s×12
HD432 (GT)	F2III	2456523.3	30s×12
		2456526.2	30s×12
HD7927 (SP)	F0Ia	2456522.3	100s×12
HD198478 (SP)	B3Ia	2456525.1	60s×12

Table 5.1 Observational log of V339 Del and several standard stars

5.3. Results

Figure 5.5 shows intensity and polarization spectra in 6 nights. P Cygni profiles which are characteristics of FeII class nova (Williams 1992) are prominent in FeIIλ6148, Hα, and OIλλ7477,7774 lines just before and after the light maximum as some authors reported (e.g., Munari *et al*. 2013, Shore *et al*. 2013a, and Tomov *et al*. 2013). NaID and HeIλ6676 show only absorption. The emission lines with P Cygni profile gradually increases after t = +3d of the maximum (Aug.19) compared to the strengths of absorption, which is due to a formation and an expansion of the emission line region by the nova wind. The Hα and OI show flat top profiles that are characteristic of N/He class nova. Thus, V339 Del has both spectral characteristics of FeII and He/Ne classes. The polarization degree of the continuum fluctuated within P = 0.2–0.3% around the maximum (t = ±1d) and after t = +2d it closed to a constant value of P ~ 0.5%. The SiIIλλ6347, 6371, Hα, and OIλλ7477, 7774 lines show the intrinsic polarizations which are different from that of the continuum. It is particularly worth noting that SiII doublet lines at t = -1d show prominent polarization in absorption, although no polarization is seen in the other lines in pre-maximum phase.

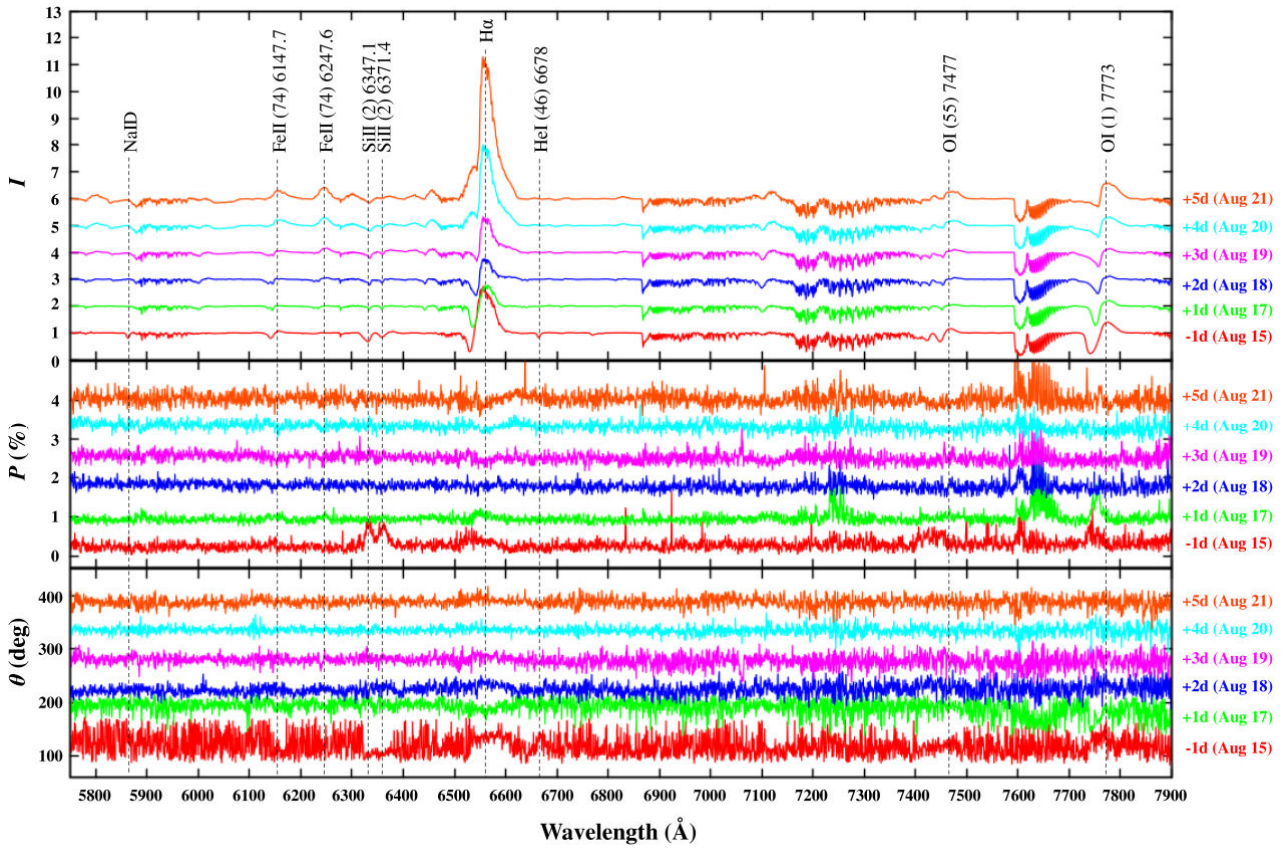

Figure 5.5 The polarization spectral evolution of V339 Del at 6 nights from Aug 15 to 21 in 2013. The top panel shows the intensity $I(\lambda)$ in arbitrary unit, the middle panel show the degree of polarization $P(\lambda)$, and the bottom panels shows the position angle $\theta(\lambda)$.

In order to investigate the variation of polarization of SiII lines in more detail, we extract the polarization spectra of SiII as Figure 5.6. It shows the intensity I, the polarized flux $I \times P$, the polarization degree P, and the position angle θ vs the heliocentric radial velocity v. The absorption of SiIIλ6347 becomes the widest (δv = 750km s^{-1}) of all observations and shows the terminal velocity of 1500 km s^{-1} at t = -1d. After the maximum, the width and the expansion velocity become gradually narrow and slow. These behaviors indicate that a prominent nova wind already had been blowing in pre-maximum phase and the SiII lines are formed optically thick nova wind with the high

velocity. In addition, the polarized flux in the absorption is stronger than that of the continuum, which indicates that the enhancement of the polarization degree in absorption is not due to an occultation effect of the light source but an actual increase of the polarized light compared to that of continuum in this phase.

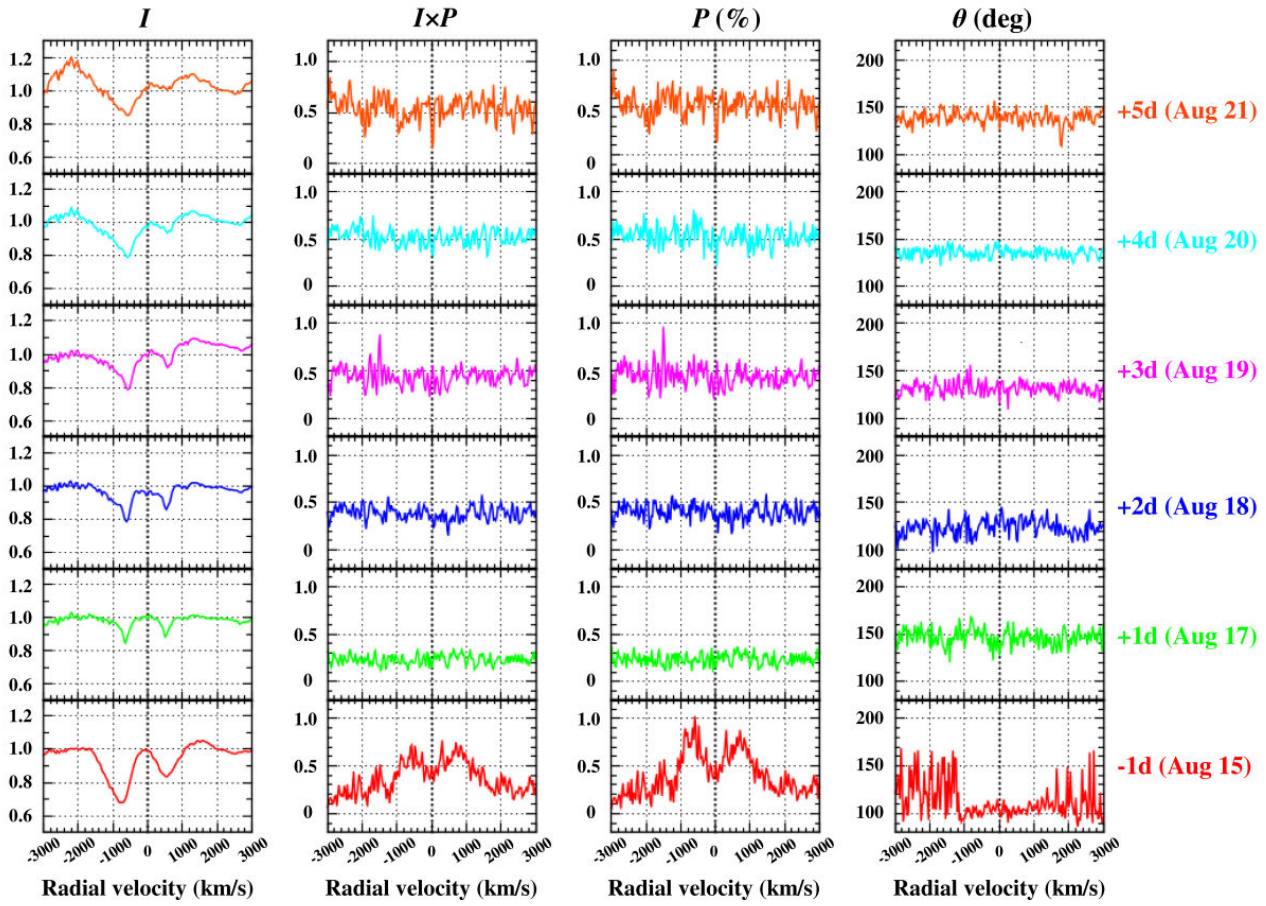

Figure 5.6 Observed spectra of SiII6347, 6371 from Aug 15 to Aug 21. From the left panel to turn show intensity I, polarized flux $I \times P$, polarization P, and polarization angle θ vs the heliocentric radial velocity v which is defined SiIIλ6347.11 as 0 km s^{-1}

Figure 5.7 shows the q-u plane in which we plot polarizations of SiII lines averaged across the absorption (at t = -1d) and the polarizations of continuum around the SiII lines from t = -1d to t = +5d. The polarizations of continuum are averages between 6400 Å and 6450 Å where any prominent spectral features are not seen either in intensity spectra or polarization spectra. The polarization of continuum shows time variation and gradually approaches a point at (q_0, u_0) = (-0.49±0.07%, 0.15±0.05%) which is interpreted as a combination of interstellar and permanent circumstellar polarization. While the position angles of both SiII lines are $\theta \sim 143°$ seen from the (q_0, u_0), those of continuum are almost $\theta \sim 160°$. The stronger polarized flux and the different position angle of SiII lines from the continuum, indicate that the distributed structure is different between SiII lines and continuum which would originate from the pseudo-photosphere and free-free emission region. We discuss the possible origins of these polarizations in next section.

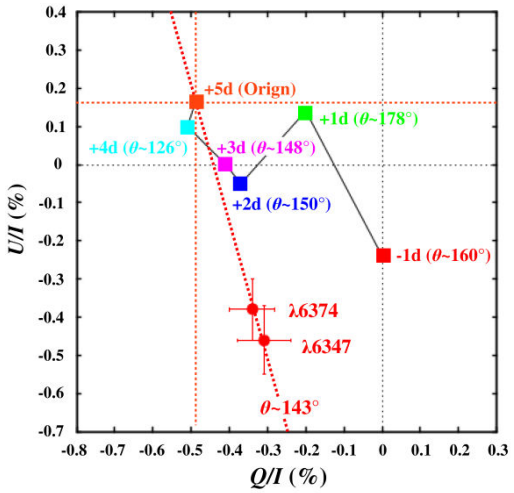

Figure 5.7 The q-u plane. The circles show the polarizations of SiII lines averaged across the absorption (at t = -1d). The squares show the polarizations of continuum around the SiII lines (from t = -1d to t = +5d).

5.4. Discussion

We detected prominent polarization in only SiII lines in pre-maximum phase of V339 Del. The polarization of SiIIλλ6347, 6371 is the first detection as far as we know (there had been few reports of even spectroscopic results on this lines except for those of Nova Cas 1995 by Iijima *et al.*(1998)). Furthermore, we detected time variability of the polarization in the continuum during a few days after -1d. These polarizations in the relatively early phase would be a clue to resolve the origin of non-spherical geometry of nova phenomenon, because the pseudo-photosphere dose not reach to the maximum radius at this phase, the light emitted from the nova could still keep much more information on the non-spherical geometry at the timing of ignition of the thermo-nuclear runaway (TNR). In this section, we discuss the time variabilities of the shape of the pseudo-photosphere and surrounding free-free emission region including the forming region of SiII lines, and the possibility of the origin of polarization.

5.4.1 The time variation of the polarized continuum

Since the atmosphere of nova near the light maximum is known to be an electron scattering dominated photosphere, the continuum is dominated by the free-free emission. Thus, the observed polarization is thought to originate from a similar mechanism as seen in an early type star, which presents a non-symmetric geometry of the pseudo-photosphere. In addition, this polarized continuum shows time variation (see Figure 5.7). It suggests an evolution of the size, geometry, and density distribution of the photosphere with the variation of the brightness of nova. The polarization degree of continuum was P = 0.63% at pre-maximum (t = -1d) and after then it gradually decreases with an almost constant polarization angle (see Figure 5.7). This would be attributed to (a) : that a strongly distorted photosphere in the early phase gradually became a sphere shape while it is shrinking (a change of the geometry), (b) : the optical thickness in the free-free emission region, which produces a strong polarization, gradually become small with the shrinking of the photosphere. With results of Monte-Calro simulations by Hoflich (1991), while the photosphere should have an oblate ellipsoid with an eccentricity e = 0.47 for the case of (a) and the photosphere should have a prorate ellipsoid with the optically thickness of τ = 5 at t = -1d (pre-maximum phase.

5.4.2 Candidate of the forming region of SiII lines

There are three candidates of forming regions of SiII lines in the radiation field of nova; (a): the inside of circumbinary matter formed in the past explosions, (b): the atmosphere or the accreting matter of the companion, and (c): the inside of WD ejecta by the latest nova explosion.

Since V339 Del has a relatively high mass WD as discussed in the later part of this section, it is easy to imagine that it exploded more than several times in the past. Therefore, it is supposed that the ejecta lost in those explosions surround the whole of binary system.

The SiII pieces in this circumbinary matter could produce absorption lines when a light source such as the pseudo-photosphere of the nova is in back of this cloud (= (a)). Williams *et al*. (2008, 2010) concluded that several absorption lines by heavy elements such as ScII, TiII, VII, CrII, and FeII, are formed in the circumbinary cloud nebula matter. This hypothesis is supported by that the line width of these absorption lines (named as "THEA system") are relatively narrow (typical line widths of ~ a few$\times$10 km s^{-1}). In contrast, SiII absorption lines we detected have the widths of ~ 750 km s^{-1} for SiIIλ6347 and ~ 560 km s^{-1} for SiIIλ6371 which are considerably wider than those of the THEM system. Therefore, it is improbable that SiII lines are formed in the circumbinary cloud.

Williams (2012) mentioned that FeII lines seen in FeII class nova are formed in the nebula which is originally the atmosphere of a companion activated by the collision to the ejecta and the γ-ray by the TNR and is lost through L1 and/or L3 points (= (b)). Figure 5.8 shows a time variation of FeIIλ6148 line profiles from Aug. 15 (t = -1d)

to 18 (t = +2d). The absorption of FeII is divided into two components (v ~200 km s^{-1} and 600 km s^{-1}) at t = +1d after it shows P Cygni profile during the pre-maximum phase. Since a component with a high velocity (v ~ 600 km s^{-1}) seems to agree with SiII line profile which is overplotted in the same figure with dashed lines, this component would originate from the same region of SiII lines. On the other hand, the other component with a lower velocity (v ~ 200km s^{-1}), could originate from the nebula proposed by Williams (2012) because the expansion velocity which is near an escape velocity determined by the gravity field in the Roche potential, would be very slow. Therefore, the gas from the companion could not be a main emitting region of SiII lines.

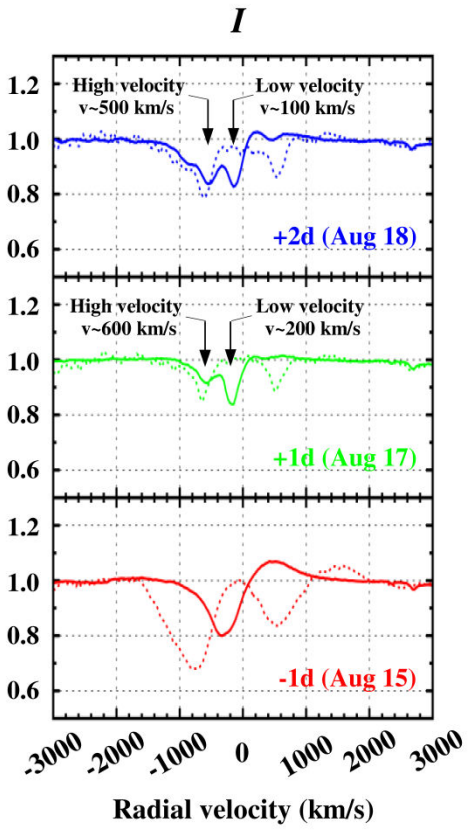

Figure 5.8 The line profiles of FeIIλ6148 lines (solid lines) and SiII (dashes lines) at three timings, t = -1d, +1d, and +2d. The horizontal axis is the heliocentric radial velocity v,

and the vertical axis is the intensity *I* in arbitrary units.

If most SiII lines would be formed in the WD ejecta (= (c)), the line profiles should show a behavior of a high activity related to the pseudo-photosphere and/or the nova wind. According to Williams *et al*. (2008), spectral lines from the WD ejecta shows the expansion velocities of 1000–2000 km s^{-1} typically. SiIIλλ6347,6371 show P Cygni profiles with the terminal velocity of ~ 2000 km s^{-1} at *t* = -2d (Shore *et al*. 2013a) and ~1600 km s^{-1} at *t* = -1d (see figure.5.6), respectively. Those results strongly support that SiII lines are generated in the WD ejecta. By the way, it is an attractive question where the Si species comes from, because there are a small number of novae showing strong SiII lines as above mentioned, which might be related to the origin of the non-spherical geometry. Jose & Mernanz (1998) suggest that a large amount of Si atoms including three isotopes ^{28}Si, ^{29}Si, and ^{30}Si, are generated by the TNR on the ONe-core WD which would be evolved from a CO-core WD. Generally, the mass of ONe-core WD is thought to be higher than 1.35 $M_{\odot}$ (Jose *et al*.2001). Therefore, we can verify this possibility by investing the WD mass of V339 Del, It is well known that WD mass of nova (M_{WD}) is strongly related to the decline time t_3 and the maximum absolute magnitude. Livio (1992) propose two empirical relations on the WD mass as follows,

$$t_3 = 51.3\left[\frac{M_{WD}}{M_c}\right]^{-1}\left[\left(\frac{M_{WD}}{M_c}\right)^{-2/3} - \left(\frac{M_{WD}}{M_c}\right)^{2/3}\right]^{3/2} \qquad (1)$$

$$M_B{}^{max} \sim M_V{}^{max} = -8.3 - 10.0\log\frac{M_{WD}}{M_{\odot}} \qquad (2)$$

where M_c is the Chandrasekhar mass, $M_B{}^{max}$ and $M_V{}^{max}$ are the absolute magnitudes at maximum for *B*-band and *V*-band, respectively. The calculated WD masses are $M_{WD} \sim 1.08 M_{\odot}$ using Eqs. (1) and t_3 = 18day (Chochol *et al*.

2014), and $M_{WD} \sim 1.10 M_{\odot}$ using Eqs. (2) and M_V^{max} = -8.70±0.03 (Chochol *et al.* 2014). The estimated mass is in good agreement with earch other and does not reach the mass limit of ONe-core WD, 1.35 $M_{\odot}$. Therefore, there is an excellent possibility that V339 Del has not a ONe-core WD but a CO-core WD, and the Si species is initially included in the accreting gas from the companion (although we cannot reject a possibility that the WD mass are gradually decreasing by several nova explosions in the past after a high mass ONe-core was generated at once).

We conclude that SiII lines is mainly formed in the WD ejecta (= (c)) and the Si species is not generated in the TNR but is originally included in accreting gas from the companion.

5.4.3 Origin of polarization in SiII lines

We discuss the origin of polarization in SiII lines. As seen in Figure 5.4, the position angle is apparently different between continuum and SiII lines at t = -1d by 17 degree. And, the polarized fluxes of SiII lines are enhanced compared to that of continuum at the same timing (see Figure 5.3). These indicate that the SiII emitting region would be non-uniformly distributed on the pseudo-photosphere (see Figure 5.9). If SiII region is locally on the pseud-photosphere, SiII lines should have a polarization with a different position angle from the continuum because a part of polarized light is left without compensation due to the absorption of a polarized flux with a certain position angle. Kawabata *et al*. (2002) also suggests that the difference of the position angle between CaII triplet lines and OI line, which is observed in SN2002ap, would be due to the difference of the spatial distribution on the pseud-photosphere. The disappear of polarization of SiII in the post maximum phase can be explained as the attenuation of polarization due to the expansion of the SiII region.

If the SiII region is locally distributed on the pseudo-photosphere in the pre-maximum phase, the SiII already has been localized just after or at the timing of TNR. As mentioned in the previous subsection, since Si species should not be generated by nuclear reaction, a hypothesis that the SiII is locally synthesized on the surface on the WD by TNR is rejected. A possible hypothesis is the diffusion of Si species in the atmosphere of the WD. The first nuclear reaction is thought to be ignited on at a local region of the bottom layer in the hydrogen atmosphere. If Si species sinks to the bottom of the hydrogen layer by diffusion, Si species could be selectively brown to the

outer region by the first ignition. In the early phase of nova explosion, we might observe a small ejecta including a large amount of Si species, which would be released in a random direction. Since the degree of diffusion should be different between species, it is easy to explain a reason why there is no polarization observed in other lines except for SiII lines in the pre-maximum phase (A slight polarization seen in OI lines might support this hypothesis because O species is also ejected from the inner layer of the WD).

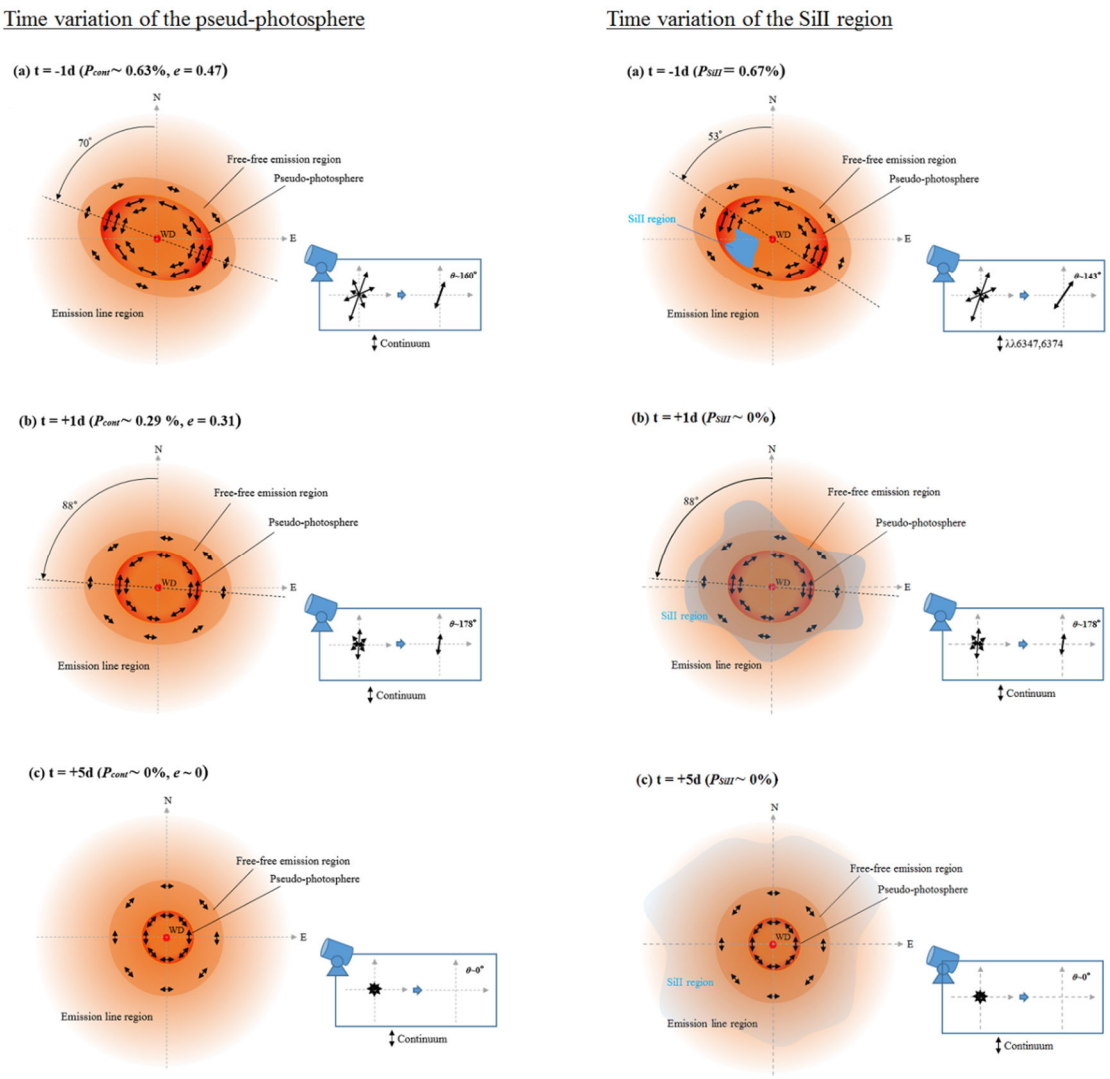

Figure 5.9 Schematic representation of the time variation of the pseud-photosphere (left figures) and SiII region (right figures). (a), (b), and (c) are t = -1d, +1d, and +5d, respectively. As seen in the left figures, there show the time variation of the photosphere with a polarization fluctuations. Each of the asymmetric structures (= eccentricity e) are described based on Holfich (1991). As seen in the right figures, there should have a polarization with a different position angle from the continuum at t = -1d by the SiII region which is non-uniformly distributed on the pseudo-photosphere. Because the SiII region spread after pre-maximum, it did not contribute to the polarization.

5.5 Conclusion

We carried out a monitoring observation of V339 Del with a high resolution spectro-polarimeter, VESPolA, attached to the 1.3m Araki telescope of Koyama Astronomical Observatory. We confirmed the nova wind even in the pre-maximum phase, from P Cygni profiles seen in FeIIλ6148, SiIIλλ6347, 6371, Hα, and OIλλ7477, 7774 lines. We also detected the intrinsic polarizations in the SiIIλλ6347, 6371, Hα, and OIλλ7477, 7774 lines. It is particularly worth noting that only SiII doublet lines at t = -1d show a prominent polarization in absorption, although no polarization is seen in the other lines. This polarization would reflect a patched or biasedly distribution of the SiII region on the pseudo-photosphere. This suggests that the first nuclear reaction is locally ignited in the bottom of hydrogen layer of the WD atmosphere, into which the Si species is diffused. This Si species is not generated by the TNR but is originally included in accreting gas from the companion.

6. Summary

We succeeded in development of high resolution spectro-polarimeter,VESPolA, for study on spatial distribution and velocity field of circumstellar matters. The system, which exploits new devices together with recent techniques developed for spectro-polarimeters for use with 8–10 -m class telescopes, was mounted on the 1.3 -m Araki-telescope at Koyama Astronomical Observatory. We evaluated the performances of the system, and conclude that VESPolA achieves a spectral resolution of $7,750 < R < 8,250$, polarimetric accuracy of $\delta P \sim 0.1\%$ ($P < 6\%$) for linear polarization, and limiting magnitude of $m_v = 7.8$ mag, with $\delta P < 0.1\%$ and an integration time of 4 hours. Therefore, the observation accuracy could be shown that it was effective enough for desired much science of nova using VESPolA.

We carried out a monitoring observation of V339 Del and confirmed from P Cygni profiles in FeII, SiII, HeI, OI, and Balmer lines that the nova wind already has just before the maximum. In addition, the SiIIλλ6347, 6371, Hα, and OIλλ7477, 7774 lines show the intrinsic polarizations which is different from that of the continuum. In particular, only SiIIλλ6347, 6371 show prominent polarization in the pre-maximum phase. This polarization would reflect a patched or biasedly distribution of the SiII emission region on the pseudo-photosphere. This suggests that the first nuclear reaction is locally ignited in the bottom of hydrogen layer of the WD atmosphere, into which the Si species is diffused. This Si species is not generated by the TNR but is originally included in accreting gas from the companion.

Acknowledgments

I was able to accomplish this study thanks to much support and instruction. I especially would like to my deepest appreciation to Dr. Y. Ikeda who provided considerable encouragement and invaluable discussion. I would like to thanks Prof. H.Kawakita, Dr. S. Kondo, Dr. A. Nakamichi, and Dr. N. Hujishiro for their support throughout this program. I also would like to acknowledge the developers of LIPS, especially Prof. K. S. Kawabata and Dr. H. Akitaya, for providing an opportunity to build VESPolA and for providing technical comments on the spectro-polarimeter. A. Hori, Y. Shinnaka, and C. Itose took a part in the initial phase of building VESPolA. K. Nakamura supported the estimation of the limiting magnitude of the field viewer system. I am grateful to all of the staff of Koyama Astronomical Observatory.

References

Akitaya, H., Ikeda, Y., Kawabata, K., *et al*. 2009, A&A, 499, 163

Arasaki, T., Ikeda, Y, Shinnnaka., Y., Itose, C., *et al*. 2015, PASJ

Arasaki, T., Ikeda, Y., Nakamichi, A., Kawakita, H. 2014, SPIE, 9147, 88

Aspin, C., Schwarz, H. E., McLean, I. S. 1985, A&A, 151, 169

Calvet, Nuria., Hartmann, Lee., Herwett, Robert. 1994, ApJ, 386, 229

Catanzaro, G. 2013, A&A, 550, 79

Chochol, D., Shugarov, S. Y., Pribulla, T., Volkov, I. 2014, CoSka, 43, 330

de Diego, Jose, A., Gonzalez-Perez, Jose, N., *et al*. 1994, AAS, 184, 1707

Dhillon, V. S., Rutten, R. G. M. 1995, MNRAS, 274, 27

Donati, J. -F., Catalo, C., Wade, G.A., *et al*. 1999, A&AS, 134, 149

Donati J. -F. 2003, ASPC, 307, 41

Donati, J. F., Catala, C., Landstreet, J.D., Petit, P. 2006, ASPC, 358, 362

Downes, R. A., Duerbeck, H. W. 2000, AJ, 120, 2007

Ebizuka, N., Kawabata, K., Oka, K., *et al*. 2011, PASJ, 63, 613

Hachisu, I., Kato, M. 2014, ApJ, 785, 97

Harman, D. J., Bode, M. F., Darnley, M, J., *et al*. 2008, ASPC, 401, 246

Harries, T, J., Howarth, I, D. 1996, A&AS, 119, 61

Harries, T, J., Howarth, I, D. 2000, A&A, 361, 139

Harrington, D. M., Kuhn, J. R., Whitman, K. 2006, PASP, 118, 845

Harrington, D. M., Kuhn, J. R. 2009, ApJ, 695, 238

Hillebrandt, Wolfgan., Niemeyer J, Jeans C. 2000, ARAA, 38, 191

Hoffman, J. L., Noordsieck, K.H., Fox, G.K. 1998, AJ, 115, 1576

Hoflich, P. 1991, A&A, 246, 481

Hsu, J-C., Breger, M. 1982, ApJ, 262, 732

Iijima, T., Rosino, L., della Valle, M. 1998, A&A, 338, 1006

Ikeda, Y., Akitaya, H., Matsuda, K., *et al*. 2003, SPIE, 4843

Ikeda, Y., Akitaya, H., Matuda, K., et al. 2004, ApJ, 604, 357

Ilyin, I., Strassmeier, K.G., Woche, M., *et al*. 2011, Astron. Nachr, 332, 753

Jose, Jordi., Hernanz, Margarita. 1998, ApJ, 494, 680

Jose, Jordi., Coc, Alain., Hernanz, Margarita. 2001, ApJ, 560, 897

Kashikawa, N., Aoki, K., Asai, R., *et al*. 2002, PASJ, 54, 819

Kawabata, K. S., Okazaki, A., Akitaya, H., *et al*. 1999, PASP, 111, 898

Kawabata, K. S., Akitaya, H., Hirakata, N., *et al*. 2001, ApJ, 552, 782

Lasker, B. M., Lattanzi, M. G., McLean, B. J., *et al*. 2008, AJ, 136, 735

Livio, M.1992, ApJ, 393, 516

Munari, U., Zwitter, T., Tomov, T., *et al*. 1999, A&A, 347, 39

Munari, U., Valisa, P., Milani, A., Cetrulo, G. 2013, ATel, 5297

Nomoto, K., Yamaoka, H., Shigevama, T., *et al*. 1994, supe.conf, 199

Pereira, A., di Cicco, D., Vitorino, C., Green, D. W. E. 1999, IAU, Circ, 7327

Pereyra, A., de Arauio, F. X., Magalhaes, A. M., *et al*. 2009, A&A, 508, 1337

Pontefract, M., Drew, J., Harries, T., Oudmaijer, R. D. 2000, MNRA, 319, 19

Rasilla, J. L., Garcia Marin, A., Arribas, S., *et al*. 1993, ASPC, 37, 203

Schroeder, D. J. 2000, Astronomical optics, 2nd ed., Academic Press: New York

Schmid, H. M. 1989, A&A, 211, 31

Schmid, H. M., Schild, H. 1990, A&A, 236, 13

Schmidt G. D., Elston, R., Lupie, O. L., 1992, AJ, 104, 1563

Seifert, W., Appenzeller, I., Fuertig, W., *et.al*. 2000, SPIE, 4008, 96

Serkowski, K. 1974, Astrophysics: Optical and nfrared in Methods of Experimental Physics, Vol. 12, Part A (Ed. N.Carleton)

Shore, S. N., Shoda, P., Rutsch, P. 2013a, ATel, 5282

Schmid, H, M.1989, A&A, 211, 31

Schumid, H, M., Schild, H. 1994, A&A, 281, 145

Schumid, H, M., Schild, H. 1997, A&A, 327, 219

Silvester, J., Wade, G. A., Kochukhov, O., Bagnulo, S., *et al*. 2012, MNRAS, 426, 1003

Snik, F., Kochukhov, O., Piskunov, N.*, et al*. 2011, ASPC, 437, 237

Smith, Nathan., Hartigan, Patick. 2006, ApJ, 638, 1045

Smith, N. 2008, ASPC, 388, 129

Stahl, O., Mande, H., Wolf, B., *et al*. 1993, A&AS, 99, 167

Takami, M., Bailey, J., Gledhill, T. M., *et al*. 2001, MNRAS, 323, 177

Taylor, M., Nordsieck, K. H., Schulte-Ladbeck, R. E.,Bjorkman, K.S. 1991, AJ, 102, 1197

Tomov, T., Ilkiewicz, K., Swierczynski, E., *et al*. 2013, ATel, 5288

Turnshek, D. A., Bohlin, R. C., Williamson, R. L., *et al*. 1990, AJ, 99, 1243

Vink, Jorick. S., Drew, J. E., Harries, J. E., *et al*. 2003, A&A, 406, 703

Yoshikawa, T., Ikeda, Y., *et al*. 2012, SPEI, 8444, 84456G

Waagen, E. O. 2013, *AAVSO Alert Notice*, 489

Williams, Robert. 1992, AJ, 104, 725

Williams, Robert., Mason, Elena., Della, Valle., *et al*. 2008, ApJ, 685, 451

Williams, Robert., Mason, Elena. 2010, Ap&SS,327, 207

Williams, Robert. 2012, AJ, 144, 98

Whittet, D. C. B., Martin, P. G., Hough, J. H., *et al*. 1992, ApJ, 386, 562

Wolff, M. J., Anderson, C. M., Clayton, G., *et al*. 1996, AAS, 28, 914

Wood, K., Brown, J.C., Fox, G.K. 1993, A&A, 271, 492

Woudt, P. A., Steeghs, D., Karovska, M., *et al*. 2009, ApJ, 706, 738

Appendix

A. Various spectro-polarimetric spectra by VESPolA

We show the observation results of interesting stars that was observed by VESPolA.

A.1. P Cyg

LBV is thought as an evolved massive star from O-type main sequence star. It continues to lose the mass due to by the radiation pressure close to the Eddington limit and evolves a supernova triggered by the gravitational collapse through the WR star phase. In addition, LBV star is known to vary the brightness irregularly with time scales form a few hours to a few hundred years. These variations often accompanied with an explosion phenomenon, which would be related to the massive mass loss by the stellar wind or a temporal small explosion called as “eruption” (e.g., Smith 2008). Because LBV star losses almost of the hydrogen outer-atmosphere in the short life time of ~ 10^4 years before WR stars, this mass loss process should be directly related to stellar evolution. P Cygni belongs to LBV star and the short timescale variation of day-to-week is interpreted as the temporal insubstantial mass loss event (Nordsieck *et al*. 2001). We carried out the spectro-polarimetric monitoring using VESPolA form August 2013 to November 2013. As a result, we found temporal variations in the polarization spectra along the absorption of P Cygni profiles including Hα and HeI (667.6 nm). This result might support that the temporal insubstantial eruptions, which would be lost to the tangential direction in the celestial coordinate, because the time variation of emission lines are not seen.

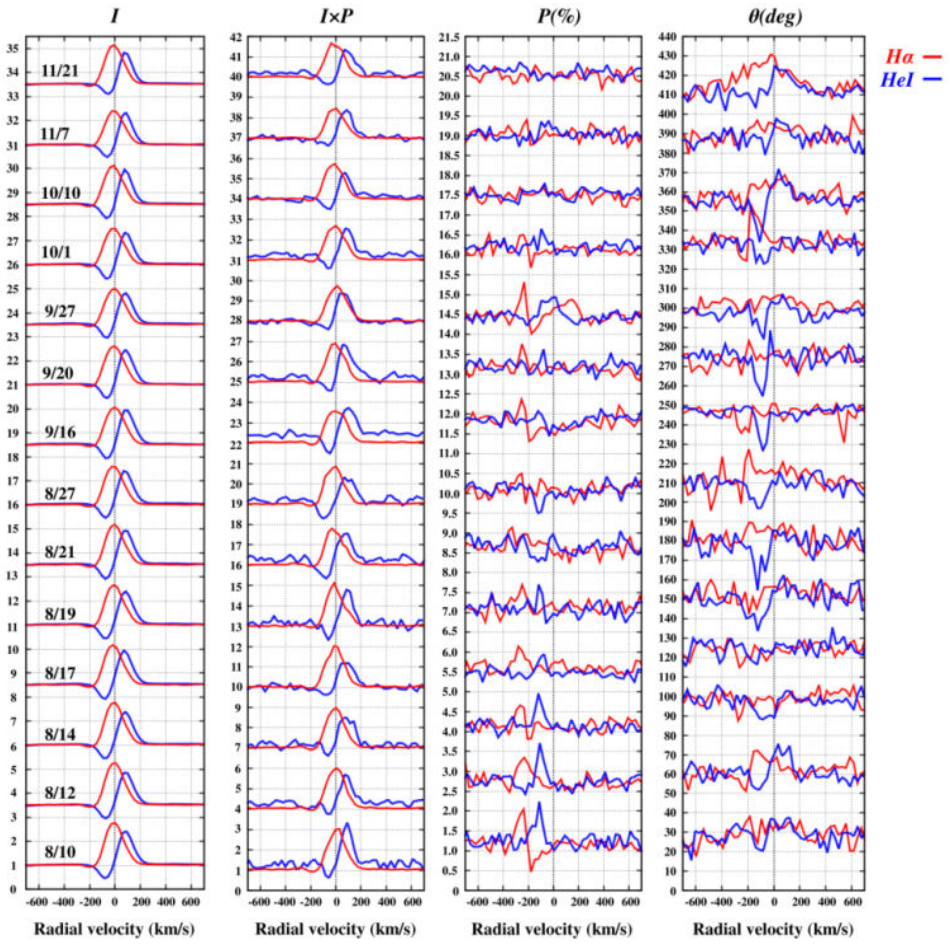

Figure A.1 Observed spectra of Hα (red) and HeIλ6677(blue) of P Cygni from 2013 August 11 to November 21. The leftmost panel raw intensity I, the second is polarized flux $I \times P$, the third is polarization P, and the rightmost is polarization angle θ. The horizontal axis of all figures are heliocentric radial velocity v (km/s).

A.2. β Lyrae

β Lyrae is an eclipsing binary star which consists of two B-type stars (B0.5V for a primary and B6-8II for a companion, Hoffman *et al*. 1998). The orbital period is 12.9 day. It is thought that since the companion fill its Roche lobe, a part of the atmosphere flow to the primary star via the L1 point and forms the accretion disk around the primary star (Bonneau *et al*. 2011). β Lyrae shows complicated profiles in hydrogen and helium lines with the time variation, which synthesizes the orbital motion. However, the mechanism which would reflect the complicated geometry and the velocity field inter and inner binary region, is still an open issue. We carried out a monitoring observation using of β Lyrae using VESPolA on Aug 2013. This observational set entirely covers one orbital period. We can see a periodic variation in polarized emission lines. By analyzing these polarization spectra, we can extract much information on the complicated geometry of the circumbinary nebular in β Lyrae (Figure A.2).

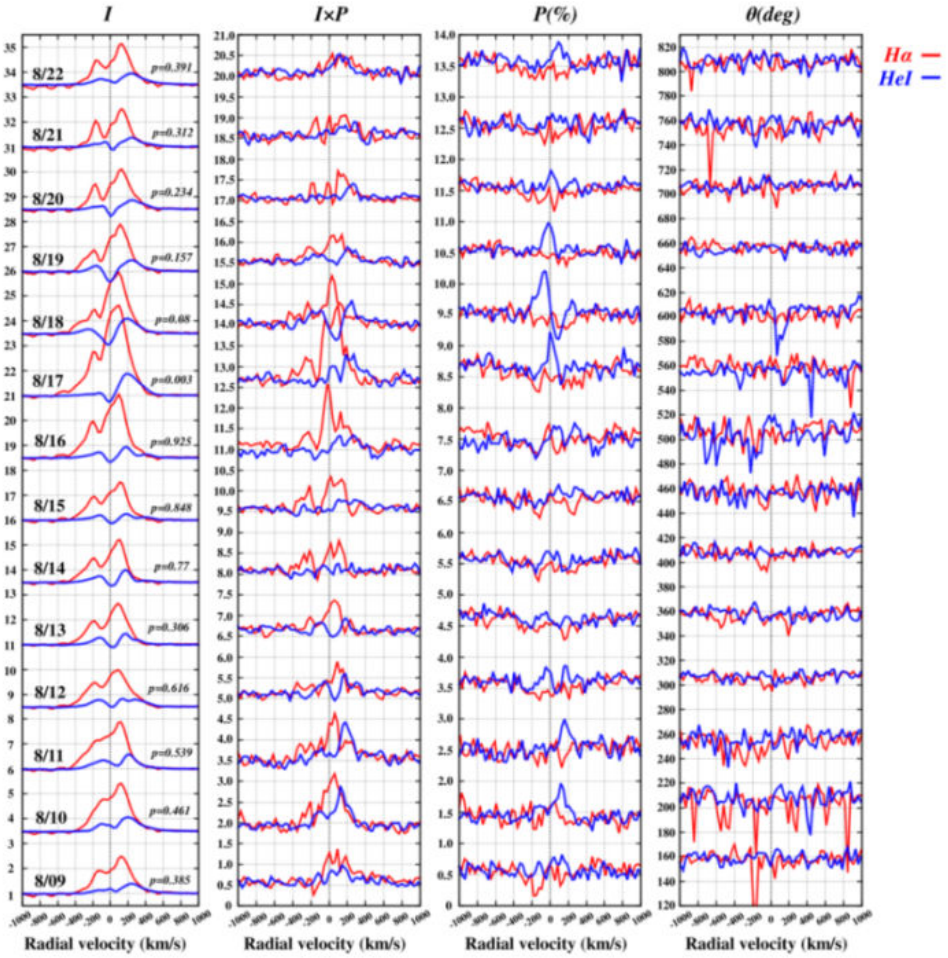

Figure A.2 Observed spectra of Hα (red) and HeIλ6677(blue) of β Lyrae. The horizontal axis and the vertical axes are similar as Figure A.1.

A.3. VY CMa

VY CMa is a luminous red supergiant (M5eIa) with the mass 30–40$M_{\odot}$. It is thought to evolve to gravitational collapse type II type SN in near future. VY CMa is surrounded by dense circumstellar matters distributed asymmetrically. From multi-photometric observations, it is considered that VY CMa has a disk and jet structure (Kastner and Weintraub 1998). Furthermore, it also shows a large linear-polarization of more than 10% in the visible and infrared continuum, which strong supports an asymmetry of the circumstellar matter (Aspin *et al*. 1985). We took the polarization spectra of VY CMa using VESPolA on November 19, 213. The polarization spectra show significant depolarizations in TiO-band (see Figure A.3), which is a similar result by Aspin *et al*. (1985). The depolarizations are also seen in neutral metal lines such as NaI, CaI, and KI. These results would be deeply related to the spatial distribution of circumbinary matters of evolved supergiant stars.

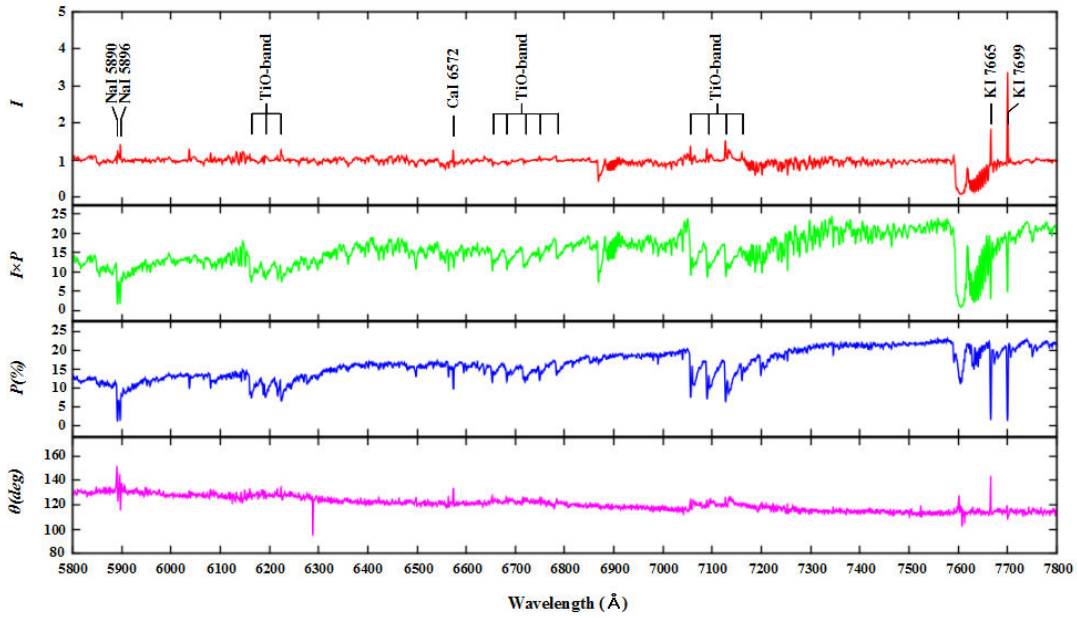

Figure A.3 Observed spectra of VY CMa.

B. Stokes parameters and Muller matrix

B.1. Stokes parameters

Light is written as a propagation of electromagnetic wave which vibrates perpendicular to the propagating direction. Thus, the light wave has two isolate modes on the vibrating direction and an arbitrary electromagnetic wave can be represented as a superposition of these two electromagnetic vectors which are perpendicular to each other. Polarization can be interpreted as a condition with unevenness among two modes. In other words, a state of polarization gives a vibrating angle and the difference on the phase between two modes of the electromagnetic wave. Each component of electromagnetic vectors, is depending the time *t*, is presented by

$$E_l = E_{l0}\sin(\omega t - \varepsilon_l) \qquad \text{(B. 1.1)}$$

$$E_r = E_{r0}\sin(\omega t - \varepsilon_r) \qquad \text{(B. 1.2)}$$

where ω is angular frequency and E_{l0}, E_{r0}, ε_l, and ε_r are amplitudes and phases. For the coherent case, a superposition of these two vectors draws an ellipse (see Figure B.1). There denote by θ the angle which the long axis of an ellipse makes to direction *l*, and by β an angle whose tangent is the ratio of the axes of the ellipse. When expressed as $tan\beta$ using angle β which is ratio of the major axis and a minor axis, $\beta = 0°$ and $45°$ is fully linear polarization and fully circular polarization. Otherwise, it becomes elliptically polarization.

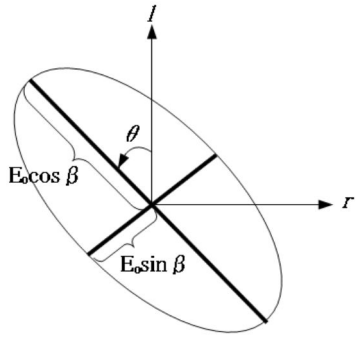

Figure B.1 Definition of a polarization

A polarization state is also represented by Stokes parameters (*I*, *Q*, *U*, *V*) instead of using $E_{l0}, E_{r0}, \varepsilon_l$, and ε_r which are constituted electromagnetic vectors. The Stokes parameters are given by

$$I = \frac{1}{2}\left({E_l}^2 + {E_r}^2\right) = Q^2 + U^2 + V^2 \qquad \text{(B. 1.3)}$$

$$Q = \frac{1}{2}\left({E_l}^2 - {E_r}^2\right) = Icos2\beta cos2\theta \qquad \text{(B. 1.4)}$$

$$U = -E_l E_r \cos(\varepsilon_l - \varepsilon_r) = Icos2\beta siin2\theta \qquad \text{(B. 1.5)}$$

$$V = -E_l E_r \sin(\varepsilon_l - \varepsilon_r) = Isin2\beta \qquad \text{(B. 1.6)}$$

where β is a ratio of the major axis and a minor axis of the elliptical polarization and θ is a polarization angle (Figure B.1). I present the intensity of electromagnetic wave, *Q*, and *U*, present linear polarization, and V presents the circular polarization. The Stokes parameters are more useful than the Jones vector which is often used to express polarization state, because Stokes parameters can express a state of partially polarization.

The *l* axial in Figure B.1 is defined as the meridian in astronomy. A polarization degree *P* and a polarization angle θ are given by

$$P = \frac{\sqrt{Q^2 + U^2 + V^2}}{I} \qquad \text{(B. 1.7)}$$

$$\theta = \frac{1}{2} tan^{-1}\left(\frac{U}{Q}\right) \qquad \text{(B. 1.8)}$$

where θ is the angle between the major axis and the meridian.

B.2. Mueller matrix

One of the matrix has the Mueller matrix that describe polarization properties of the optical elements such as a polarizer. Mueller matrix is 4×4 matrix and can obtain Stokes vector of the emitted light by triggering it in the Stokes vector of the incident light. Therefore, the Muller matrix of the optical system that there are multiple optical elements is provided by the product of individual Muller matrix.

B.2.1. Muller matrix of linear polarization

Mueller matrix of the linear polarizer which has a transmission axis of *l*-axis direction is expressed by Eq.(B.2.1) and Mueller matrix of the polarizer which has a transmission axis in φ direction is expressed by Eq.(B.2.3) using Eq.(B.2.2) which is rotation matrix：$T(\varphi)$. Thus, Stokes vector of the emitted light passing through the polarizer (I', Q', U', V') is obtained by Eq.(B.2.4).

$$M_l = \frac{1}{2}\begin{pmatrix} 1 & -1 & 0 & 0 \\ -1 & 1 & 0 & 0 \\ 0 & 0 & 0 & 0 \\ 0 & 0 & 0 & 0 \end{pmatrix} \qquad \text{(B. 2.1)}$$

$$T(\varphi) = \frac{1}{2}\begin{pmatrix} 1 & 0 & 0 & 0 \\ 0 & cos2\varphi & sin2\varphi & 0 \\ 0 & -sin2\varphi & cos2\varphi & 0 \\ 0 & 0 & 0 & 0 \end{pmatrix} \qquad \text{(B. 2.2)}$$

$$M_l' = T(\varphi) M_l T(-\varphi) \qquad \text{(B. 2.3)}$$

$$\begin{pmatrix} I' \\ Q' \\ U' \\ V' \end{pmatrix} = \frac{1}{2} T(-\varphi) \begin{pmatrix} 1 & -1 & 0 & 0 \\ -1 & 1 & 0 & 0 \\ 0 & 0 & 0 & 0 \\ 0 & 0 & 0 & 0 \end{pmatrix} T(\varphi) \begin{pmatrix} I \\ Q \\ U \\ V \end{pmatrix} \qquad \text{(B. 2.4)}$$

B.2.2. Muller matrix of retardation plate

Mueller matrix of retardation plate which has the optical axis along the *l*-axis is expressed by Eq. (B.2.5) where τ is a retardance, in the case of half-wave plate and quarter-wave plate are τ = 180° and 90°, respectively. Thus, Mueller matrix of a wave plate which has a rotation axis in φ direction is expressed by Eq.(B.2.6) using $T(\varphi)$ and Stokes vector of the emitted light passing through this wave plate (I', Q', U', V') is obtained by Eq.(B.2.7)

$$M_{WP} = \begin{pmatrix} 1 & 1 & 0 & 0 \\ 1 & 1 & 0 & 0 \\ 0 & 0 & cos\tau & sin\tau \\ 0 & 0 & -sin\tau & cos\tau \end{pmatrix} \qquad \text{(B. 2.5)}$$

$$M'_{WP} = T(\varphi) M_{WP}\, T(-\varphi) \qquad \text{(B. 2.6)}$$

$$\begin{pmatrix} I' \\ Q' \\ U' \\ V' \end{pmatrix} = T(-\varphi) \begin{pmatrix} 1 & 1 & 0 & 0 \\ 1 & 1 & 0 & 0 \\ 0 & 0 & cos\tau & sin\tau \\ 0 & 0 & -sin\tau & cos\tau \end{pmatrix} T(\varphi) \begin{pmatrix} I \\ Q \\ U \\ V \end{pmatrix} \qquad \text{(B. 2.7)}$$

C. Description of polarization light through VESPolA

VESPolA separates a stellar light, which is modulated by a half wave plate before the slit, to two polarization components (o-ray and e-ray) by a Double Wollaston prism (see Section 2.2.1). The Mueller matrix of these two optical elements are expressed as follows :

$$M_{HWP} = \begin{pmatrix} 1 & 0 & 0 & 0 \\ 0 & cos^2 2\psi + sin^2 2\psi cos\tau & (1-cos\tau)cos2\psi sin2\psi & -sin2\psi sin\tau \\ 0 & (1-cos\tau)cos2\psi sin2\psi & sin^2 2\psi + cos^2 2\psi cos\tau & cos2\psi sin\psi \\ 0 & sin2\psi sin\tau & -cos2\psi sin\tau & cos\tau \end{pmatrix} \quad (C.1)$$

$$M_{DWP} = \frac{1}{2}\begin{pmatrix} 1 & cos2\varphi & sin2\varphi & 0 \\ cos2\varphi & cos^2 2\varphi & cos2\varphi sin2\varphi & 0 \\ sin2\varphi & sin2\varphi cos2\varphi & sin^2 2\varphi & 0 \\ 0 & 0 & 0 & 0 \end{pmatrix} \quad (C.2)$$

where ψ, τ, and φ are position angle of the optical axis of half-wave plate, and retardance of a wave plate (τ = 180° in the case of the half-wave plate), and azimuth angle of the analyzer, respectively. φ is 0° for o-ray and 90° for e-ray. Therefore, the total Mueller matrix of polarization unit of VESPolA is expressed as follows :

$$M(\lambda,\psi) = M_{HWP} \times M_{DWP}$$

$$= \frac{1}{2}\begin{pmatrix} 1 & cos4\varphi & sin2\varphi & 0 \\ cos2\varphi & \frac{1}{2}cos4(\psi-\varphi)+\frac{1}{2}cos4\psi & \frac{1}{2}sin4(\psi-\varphi)+\frac{1}{2}sin4\psi & 0 \\ sin2\varphi & -\frac{1}{2}sin4(\psi-\varphi)+\frac{1}{2}sin4\psi & \frac{1}{2}cos4(\psi-\varphi)-\frac{1}{2}cos4\psi & 0 \\ 0 & 0 & 0 & 0 \end{pmatrix} \quad (C.3)$$

A light with the Stokes parameters (*I, Q, U, V*) which enters the polarization unit are converted to,

$$\begin{pmatrix} I' \\ Q' \\ U' \\ V' \end{pmatrix} = \frac{1}{2}\begin{pmatrix} 1 & cos4\varphi & sin2\varphi & 0 \\ cos2\varphi & \frac{1}{2}cos4(\psi-\varphi)+\frac{1}{2}cos4\psi & \frac{1}{2}sin4(\psi-\varphi)+\frac{1}{2}sin4\psi & 0 \\ sin2\varphi & -\frac{1}{2}sin4(\psi-\varphi)+\frac{1}{2}sin4\psi & \frac{1}{2}cos4(\psi-\varphi)-\frac{1}{2}cos4\psi & 0 \\ 0 & 0 & 0 & 0 \end{pmatrix}\begin{pmatrix} I \\ Q \\ U \\ V \end{pmatrix} \quad (C.4)$$

Therefore, the intensity spectra ($I_o{}'(\lambda,\psi)$ and $I_e{}'(\lambda,\psi)$) for o- and e-ray are obtained with $\varphi = 0°$ and $90°$ for Eq. (C.4) as follows :

$$I_o'(\lambda,\psi) = \frac{1}{2} I \left(1 + \frac{Q}{I} cos4\psi + \frac{U}{I} sin4\psi\right) \qquad (C.5)$$

$$I_e'(\lambda,\psi) = \frac{1}{2} I \left(1 - \frac{Q}{I} cos4\psi - \frac{U}{I} sin4\psi\right) \qquad (C.6)$$

These spectra, which are dispersed by the spectrometer unit, are detected on the detector. We can obtain *Q/I* and *U/I* on linear polarization by some operations with Eqs.(C.5) and (C.6) (see Appendix D).

D. Derivation of *Q*/*I* and *U*/*I* by "four-angles method"

The "four-angles method" which is used data reduction of VESPolA is a method to extract Stokes parameters (*Q/I* and *U/I*) of linear polarization from four data in one set which obtained different angle of HWP, i.e., $\psi = 0°, 45°, 22°.5, \text{and } 67°.5$ (see Section 3). One set of observation data is consisted eight spectra in total. The observed $I_o{}'(\lambda, \psi)$ and $I_e{}'(\lambda, \psi)$ which are spatially separated in the instrument by Double Wollaston prism are caught difference throughput because optical path of two rays trace which reach the detector are different. In addition, the four spectra of each position angle of HWP include the influence of environmental variations such as the weather because their spectra are obtained at different times. Therefore, the final observation data include such effects and expressed as follows :

$$I_o'(\lambda, 0°) = \frac{1}{2} I(1+q) S_o(\lambda) \eta(t_1) \qquad (D.1)$$

$$I_e'(\lambda, 0°) = \frac{1}{2} I(1-q) S_e(\lambda)\, \eta(t_1) \qquad (D.2)$$

$$I_o'(\lambda, 22°.5) = \frac{1}{2} I(1+u) S_o(\lambda) \eta(t_2) \qquad (D.3)$$

$$I_e'(\lambda, 22°.5) = \frac{1}{2} I(1-u) S_e(\lambda) \eta(t_2) \qquad (D.4)$$

$$I_o'(\lambda, 45°) = \frac{1}{2} I(1-q) S_o(\lambda) \eta(t_3) \qquad (D.5)$$

$$I_e'(\lambda, 45°) = \frac{1}{2} I(1+q) S_e(\lambda) \eta(t_4) \qquad (D.6)$$

$$I_o'(\lambda, 67°.5) = \frac{1}{2} I(1-u) S_o(\lambda) \eta(t_4) \qquad (D.7)$$

$$I_e'(\lambda, 67°.5) = \frac{1}{2} I(1+u) S_e(\lambda) \eta(t_4) \qquad (D.8)$$

where $S_o(\lambda)$ and $S_e(\lambda)$ are transmittance of o- and e-ray, $\eta(t)$ is time varying coefficient by variation of the

weather, and we substitute (Q/I) and (U/I) for q and u in their equations.

The advantage of using a "four-angles method" is to remove $S(\lambda)$ and $\eta(t)$ by analysis without using other calibration spectra. The ratio of o- and e-ray in each position angle is defined as $\kappa(\lambda, \psi)$ for four set spectra Eq. (D.9). Furthermore, a_1 and a_2 are defined using $\kappa(\lambda, \psi)$ (Eqs. (D.10) and (D.11)). As a result, it can obtain linear polarization, q and u, that $S(\lambda)$and $\eta(t)$ are removed (Eqs. (D.12) and (D.13)).

$$\kappa(\lambda, \psi) \equiv \frac{I'_e(\lambda, \psi)}{I'_o(\lambda, \psi)} \qquad (D.9)$$

$$a_1 \equiv \sqrt{\frac{\kappa(\lambda, 0°)}{\kappa(\lambda, 45°)}} \qquad (D.10)$$

$$a_2 \equiv \sqrt{\frac{\kappa(\lambda, 22°.5)}{\kappa(\lambda, 67°.5)}} \qquad (D.11)$$

$$q = \frac{1 - a_1}{1 + a_1} \qquad (D.12)$$

$$u = \frac{1 - a_2}{1 + a_2} \qquad (D.13)$$

E. The positional accuracy of HWP error

In order to operate the "four-angles method" is necessary to accurately rotate a HWP. We consider an effect of a repeatability error of HWP position angle $\delta\psi$ gives to polarization degree *P*. In the case of $\delta\psi$ occurs, Eqs. (C.5) and (C.6) in Appendix C are rewritten as follows :

$$I'_o(\lambda,\psi+\delta\psi)=\frac{1}{2}I\left(1+\frac{Q}{I}cos4\psi+\frac{U}{I}sin4\psi\right)-4\left(\frac{Q}{I}sin4\psi-\frac{U}{I}cos4\psi\right)\cdot\delta\psi \qquad (E.1)$$

$$I'_e(\lambda,\psi+\delta\psi)=\frac{1}{2}I\left(1-\frac{Q}{I}cos4\psi-\frac{U}{I}sin4\psi\right)+4\left(\frac{Q}{I}sin4\psi-\frac{U}{I}cos4\psi\right)\cdot\delta\psi \qquad (E.2)$$

Eqs. (E.1) and (E.2) ignore the second- and higher order for negligibly small. The according to Appendix D, the polarization degree P' which considered $\delta\psi$ is expressed as follows :

$$P'=P\sqrt{1+\frac{16qu}{P^2}\cdot\delta\psi} \qquad (E.3)$$

Once again, Eq. (E.3) ignores the second- and higher order for negligibly small. Furthermore, when we use an equation of $qu\le P^2$, we obtain a polarimetry accuracy error from $\delta P=|P-P'|$.

$$\delta P\le 8P\cdot\delta\psi \qquad (E.4)$$

The repeatability error of rotary stage (SURUGA-SEKI KXC0620) which is equipped with HWP of VESPolA is $\delta\psi=\pm 0.01°$. The measurement error of the polarization degree including $\delta\psi$ is estimated $\delta P\le(P/714)$ from Eq. (E.4). Therefore, an effect of a repeatability error of HWP position angle $\delta\psi$ gives to polarization degree *P* is negligibly small.

F. The cross-talk effect

The phenomenon which is an overlap between the edges of o- and e-ray in each other is called Cross-talk effect. This effect occurs by a spectrum expanding in the slit direction under the influence of seeing and aberration of optical system. Cross-talk effect reduces the contrast between measured intensity because the one-dimensional spectrum of o- and e-ray which was extracted from a two dimensional data includes the other polarization ingredient. As a result, this affects as false depolarization effect and reduces polarimetry accuracy of instrument. As follows, we estimate Cross-talk effect which occur in observation of VESPolA and quantitatively evaluate depolarization which can reduce polarimetry accuracy.

We suppose that $I'_o(\lambda,\psi)$ and $I'_e(\lambda,\psi)$ of observational data include Cross-talk which proportional to the intensity of each spectrum. They are expressed using ε as follows :

$$I'_o(\lambda,\psi) = \frac{1}{2}I[1 + q * cos4\psi + u * sin4\psi] + \varepsilon I_e \qquad (\mathrm{F.1})$$

$$I'_e(\lambda,\psi) = \frac{1}{2}I[1 - q * cos4\psi - u * sin4\psi] + \varepsilon I_o \qquad (\mathrm{F.2})$$

In here, a repeatability error $\delta\psi$ which was discussed in Appendix E does not consider. In addition, we consider that I_o and I_e which appear in second member of the right side are $I'_o \sim I_o$ and $I'_e \sim I_e$, respectively. Furthermore, we calculate q and u according to "four-angles method" of Appendix D. As a resolute, we obtained polarization degree P' which is considered Cross-talk effect from $\delta P = |P - P'|$.

$$\delta P = \left(\frac{2\varepsilon}{1+\varepsilon}\right)P \qquad (\mathrm{F.3})$$

We confirmed that Cross-talk effect of VESPolA is approximately 0.05% in typically (see section 4.2.4). Therefore,

the depolarization effect which is estimated from Eq. (F.3) is $\delta P = 0.01P$. It mean that if polarizatioin degree of target star is less than $P = 10\%$, $\delta P \sim 0.1\%$ which is required polarimetry accuracy in VESPolA is accomplished. In the case of polarization degree exceed 10%, it is to minimize polarimetry accuracy error by measuring quantity of Cross-talk effect in beforehand.

G. Theoretical formula of resolution

We write about drawing of theoretical equation of spectral resolution in geometrical optics which was showed in Figure 10 of Section 4.1. If we assume that $\delta\lambda$, $\delta\alpha$, and $\delta\beta$ are a resolvable wavelength difference, an incident width of slit incident angle by an opening aperture, and a diffraction width of diffraction angle, respectively, Eq. (G.1) is provided for wavelength λ from the grating equation. In addition, $\delta\alpha$ is expressed as Eq. (G.2) by geometric relations of spectroscopy.

$$\delta\beta \sim \frac{cos\alpha}{cos\beta}\delta\alpha \qquad (G.1)$$

$$\delta\alpha \sim \frac{s}{2f} \qquad (G.2)$$

where s is slit width, f is focus length of collimator lens, and $\delta\alpha, \delta\beta \ll 1$. On the other hand, when incident angle α is constant, the angular dispersion becomes $\delta\beta/\delta\lambda = m/dcos\beta cos\gamma$ using the grating equation. Therefore, the spectral resolution of the general spectrometer is expressed using as follows :

$$R = \lambda/\delta\lambda = \frac{2fm\lambda}{dscos\alpha} \qquad (G.3)$$

The spectral resolution of the central wavelength of each orders take constant value in many Echelle spectrometer including VESPolA because those spectrometer are semi-Littrow configuration (i.e., $\alpha = \beta$). However, α and β become different value as separated from a central wavelength because $\alpha \neq \beta$ in the wavelength edge of each order which decided in Free spectral range ($\Delta\lambda = \lambda/m$). The longest and shortest wavelength in each orders are expressed using $\Delta\lambda = \lambda/m$ as follows :

$$\lambda_s = \lambda_c - \Delta\lambda/2 \qquad (G.4)$$

$$\lambda_l = \lambda_c + \Delta\lambda/2 \qquad \text{(G. 5)}$$

H. Theoretical formula of throughput

Throughput is the total observation efficiency (including an efficiency of optical system and QE of detector) of the instrument. The light energy per unit wavelength to arrive a detector is expressed by Eq.(H1)

$$E_{obs} = f_\lambda \times T_{sky} \times \frac{\pi D^2}{4} \times R_{tel} \times t \times Th \qquad (\mathrm{H.1})$$

where T_{sky} is the atmospheric transmittance, D is a diameter of telescope, R_{tel} is an efficiency of telescope, t is an integration time, and Th is a throughput of optical system. On the other hand, E_{obs} is written as Eq.(H2)

$$E_{obs} = N_{ADU} \times g \times \frac{hc}{\lambda} \times \delta\lambda \,/\mathrm{QE} \qquad (\mathrm{H.2})$$

where N_{ADU} is count number which is obtained by a detector, g is a gain of detector [e/ADU], hc/λ is an energy per photon, $\delta\lambda$ is a wavelength width per pixel, and QE is a quantum efficiency of detector. Thus, a throughput is obtained by Eq.(H.3) from Eqs.(H.1)(H.2).

$$Th = \frac{N_{ADU} \times g \times \frac{hc}{\lambda} \times \delta\lambda}{f_\lambda \times T_{sky} \times \frac{\pi D^2}{4} \times R_{tel} \times t \times QE} \qquad (\mathrm{H.3})$$

In addition, the flux energy: f_λ is necessary to get throughput from observation. For example, we can get it from a photometry standard star catalogue such as http://snfactory.lbl.gov/snf/snf-specstars.htm. But, because the template data are described in AB-magnitude, it is necessary to convert it into the flux energy per unit wavelength which is expressed by Eq.(H.4).

$$f_\lambda = \frac{c}{\lambda^2} 10^{-\left(\frac{AB+48.6}{2.5}\right)} \qquad (\mathrm{H.4})$$

I. Limiting magnitude

The limiting magnitude is defined as the maximum magnitude to achieve an arbitrary S/N ratio in given integration time. The S/N ratio per 1 pixel of detector is expressed as follows :

$$\frac{S}{N} = \frac{S_i t}{N_{noise}} \qquad \text{(I. 1)}$$

where S_i is the number of the photon to arrive from a star per a unit of time and t is integration time. In addition, when we assume the photon flux of the m-magnitude star as S_m, S_i is expressed Eq. (I.2) by considering various dimming efficiency to receive before it arrives at the detector.

$$S_i = S_m \times \left(T_{sky} \times R_{tel} \times \frac{\pi D^2}{4} \times Th \times QE \right) \qquad \text{(I. 2)}$$

where T_{sky} is the atmospheric transmittance, R_{tel} is an efficiency of telescope, Th is a throughput of optical system, D is a diameter of telescope, and QE isa quantum efficiency of CCD. Eq. (I.2) is not considered to a central obstruction of telescope. S_m is expressed as follows :

$$S_m = \frac{E_0 \times 10^{-(m/2.5)} \times \delta\lambda \times a}{hc/\lambda} \qquad \text{(I. 3)}$$

where E_0 is an energy to radiate into the earth per unit of time, area, and wavelength, hc/λ is an energy per photon, $\delta\lambda$ is a wavelength width per pixel, and a is a sampling scale of slit. On the other hand, N_{noise} which is expressed Eq. (I.4) includes photon noise : Si which was derived from star light, readout noise : n_r and dark noise : n_d which were derived from detector, and background noise : n_b which was derived from the stray light except the star light or the sky.

$$N_{noise} = \sqrt{t\,\mathrm{S}_i + (a * b){n_r}^2 + (a * b)(n_d + n_b)t} \qquad \text{(I. 4)}$$

where a and b are sampling scale of slit each for wavelength direction and spatial direction and t is integration time. By using above equations, S/N can be expressed as follows :

$$\frac{S}{N} = \frac{S_m \times \left(T_{sky} \times R_{tel} \times \frac{\pi D^2}{4} \times Th \times QE \right) \times t}{\sqrt{t\, S_i + (a * b) n_r{}^2 + (a * b)(n_d + n_b) t}} \qquad \text{(I. 5)}$$

VESPolA is required to observe the photometric accuracy of 0.1% or less (S/N > 1000). We can estimate the limiting magnitude by calculating a magnitude which was achieved S/N > 1000 from Eq. (I.5). In addition, the limiting magnitude of VESPolA is estimated with integration time of 4 hours.